SOLVING NARROW-INTERVAL LINEAR EQUATION SYSTEMS IS NP-HARD

PATRICK THOR KAHL

Department of Computer Science

APPROVED:

Vladik Kreinovich, Chair, Ph.D.

Luc Longpré, Ph.D.

Mohamed Amine Khamsi, Ph.D.

Pablo Arenaz, Ph.D.
Dean of the Graduate School

to my

MOTHER and FATHER

with love

SOLVING NARROW-INTERVAL LINEAR EQUATION SYSTEMS IS NP-HARD

by

PATRICK THOR KAHL

THESIS

Presented to the Faculty of the Graduate School of

The University of Texas at El Paso

in Partial Fulfillment

of the Requirements

for the Degree of

MASTER OF SCIENCE

Department of Computer Science

THE UNIVERSITY OF TEXAS AT EL PASO

July 1996

Acknowledgements

Thanks to my advisor Dr. Forest, who made this whole work possible. He always help me to the very details of my work patiently.

Thanks to Dr. Kim. He helped and directed me a lot on accelerator physics area of my research and experiments.

Thanks to Dr. Chouffani and Dr. Freyberger for their advise and direction in the experiments.

Thanks to engineers at IAC, especially Chad, Kevin, Brian.

Thanks to my friends Oleksiy, Jason, Mayir, Carlos, Zaijing, Olga, and Misha always there when I needed them, like lifting heavy stuff, lead bricks.

Also Thanks to my friends Chris, Jack, Tony, and many others.

NOTE: This thesis was submitted to my Supervising Committee on the July 1, 2013.

Abstract

Solving systems of linear equations is a common computational problem well known to mathematicians, scientists and engineers. Several algorithms exist for solving this problem. However, when the equations contain *interval coefficients* (i.e., intervals in which the desired coefficient values are known to lie), the problem may not be solvable in any reasonable sense. In fact, it has been shown that the general problem of solving systems of linear equations with interval coefficients is NP-*hard*, i.e., extremely difficult and (it is believed) unsolvable; thus, no feasible algorithm can ever be developed that will solve all particular cases of this problem.

It turns out, though, that the widths of the interval coefficients are quite small in a large number of the linear systems having interval coefficients. This becomes readily apparent when we learn that the intervals typically come from measurements.

Any measurement of a physical quantity is limited by the precision and accuracy of the measuring device. To be of practical use, the measuring devices used in science and industry must be reasonably accurate. This implies that, for the most part, the actual values associated with measurements lie within relatively narrow intervals. Indeed, manufacturers often guarantee the error of their instruments to be very small.

Thus, we desire to look only at *narrow-interval* coefficients when considering the development of an algorithm for solving linear systems with interval coefficients. As there already exists an algorithm that solves most such systems, developing such an algorithm seems indeed promising. Therefore, the goal of this thesis is to answer the following question:

> *Can a feasible algorithm be developed for the general problem of solving systems of linear equations with narrow-interval coefficients?*

We show here that this problem, that of solving systems of linear equations with narrow-

interval coefficients, is NP-hard; thus, we do not consider it possible to develop a feasible algorithm that will solve all particular cases of this problem.

Table of Contents

Chapter 1

Introduction

1.1 Positron Beam

Positrons have many potentials in many discipline of science, like chemistry, physics, material science, surface science, biology and nanoscience [1] There are many different ways to generate positrons, and the main challenge is increasing the intensity (or current) of the positron beam.

1.2 Motivation

The nucleon electromagnetic form factors are fundamental quantities that related to the charge and magnetization distribution in the nucleon. Conventionally, the nucleon form factors are measured using Rosenbluth Technique (RT) [2]. The form factor scaling ratio,$R = \mu_p G_{Ep}/G_{Mp}$, measured using this technique is around unity as shown in the figure below [3]. Since nighties, a technique using elastic electron-proton polarization transfer to measurement this ratio have been developed [3, 4, 5]. In this technique, form factor scaling ratio linearly decreases as the the Q^2 increases, as shown in the Fig. 1.1.

The disagreement could arise from the fact the Rosenbluth Techqniue assumes that One Photon Exchange (OPE) during the scattering while the twophoton exchange (TPE), which depends weakly on Q^2, could also become considerable with increasing Q^2 [4]. The contribution of TPE can be obtained by comparing the ratio of e^+ p to e^- p ratio. The interference of OPE and TPE can also be studied in the process $e^+e^- \rightarrow p\bar{p}$

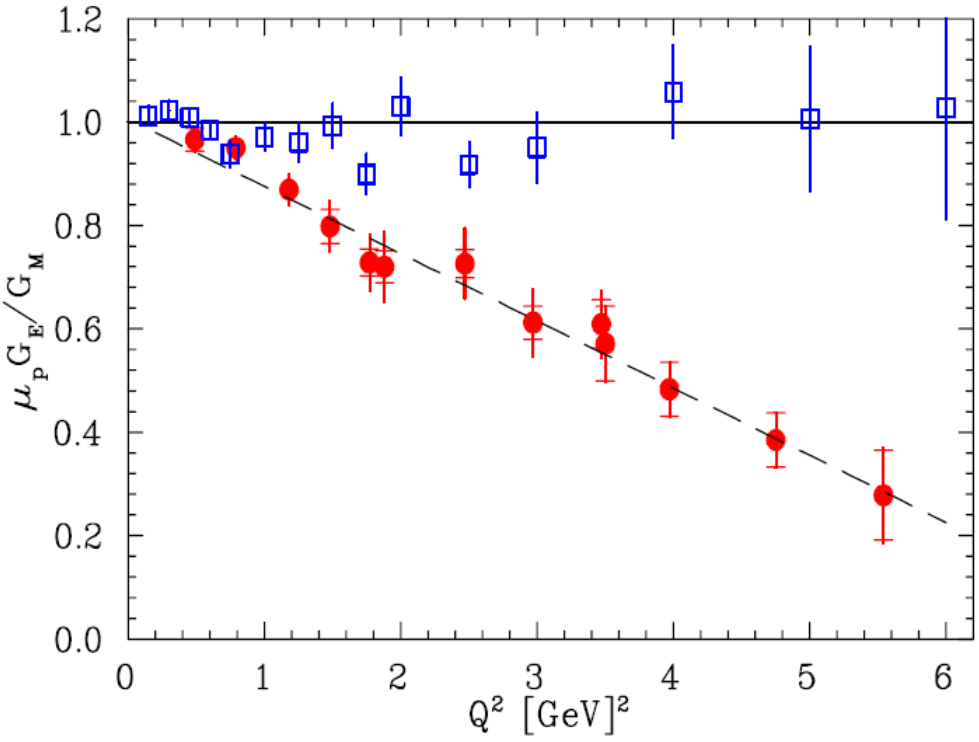

Figure 1.1: Form factor ratio, obtained by Rosenbluth Technique (hollow square) and results from Recoil Polarization Technique [4].

Chapter 2

Theory

2.1 Positron Beam Generation from Bremsstrahlung

When a moving charge particle interacts with the electric field of another charged particle, it can be deflected and releases lost energy in the form of photons, as shown in the Fig. 2.1. This is known as the Bremsstrahlung process. The probability of this interaction increases with the atomic number of the material traversed by the incident charged particle. Fig. 2.2 show the photon energy distribution when a 12 MeV electron distribution from Fig. 2.3 interacts with a 1 mm thick Tungsten target. The number of photons in this example produced decreases as the energy of the produced photon increases. The Bremsstrahlung photons are also likely to interact with the material.

There are three competing processes that a photon can undergo when interacting with matter. At electron volt (eV) energies comparable to the electron atomic binding energy, the dominant photon interaction is via photoelectric effect. As the photon energy increases up to kilo-electron volt (keV) range, the Compton scattering process starts to be more dominant. Although the photon is totally absorbed during the photoelectric effect, photons merely lose energy when undergoing Compton scattering. As the photon energy reaches twice the rest mass energy of electron, 2×511 keV, pair production begins to happen. Pair production becomes dominant interaction process only for energies above 5 MeV [6]. In this process, a photon interacts with the electric field of the nucleus or the bound electrons and decays into an electron and positron pair.

The positron and electron pairs are created back to back in the center of mass frame. In the lab frame, electrons and positrons are boosted forward, as demonstrated in the

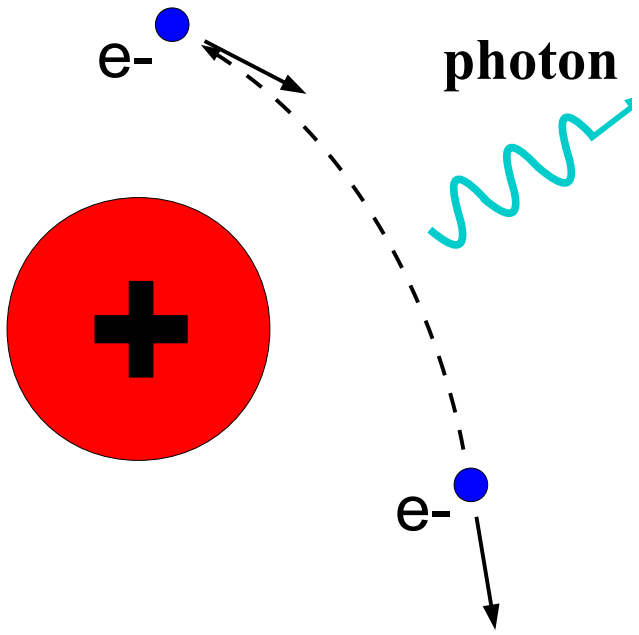

Figure 2.1: Photon generation from Bremsstrahlung processes.

Fig. 2.5. The positron and electron carry away the energy from the photon that is in excess of 1.022 MeV. In the center of mass frame, the kinetic energy is equally shared. Photons with an energy above 1.022 MeV in the bremsstrahlung spectrum of Fig. 2.7 have the potential to create electron and positron pairs. When the process of annihilation is included in the simulation, Fig. 2.8 becomes Fig. 2.9 showing a clear 511 keV peak on top of the bremsstrahlung spectrum. This 511 keV peak represents photon produced when the created positrons, from pair production, annihilates with an atomic electrons inside the tungsten target.

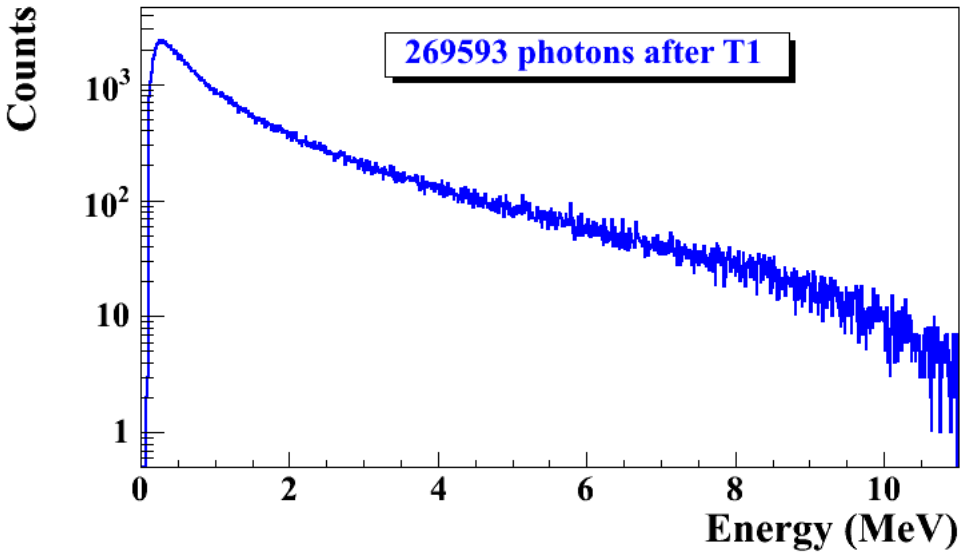

Figure 2.2: Simulated Bremsstrahlung photon energy right after a tungsten foil.

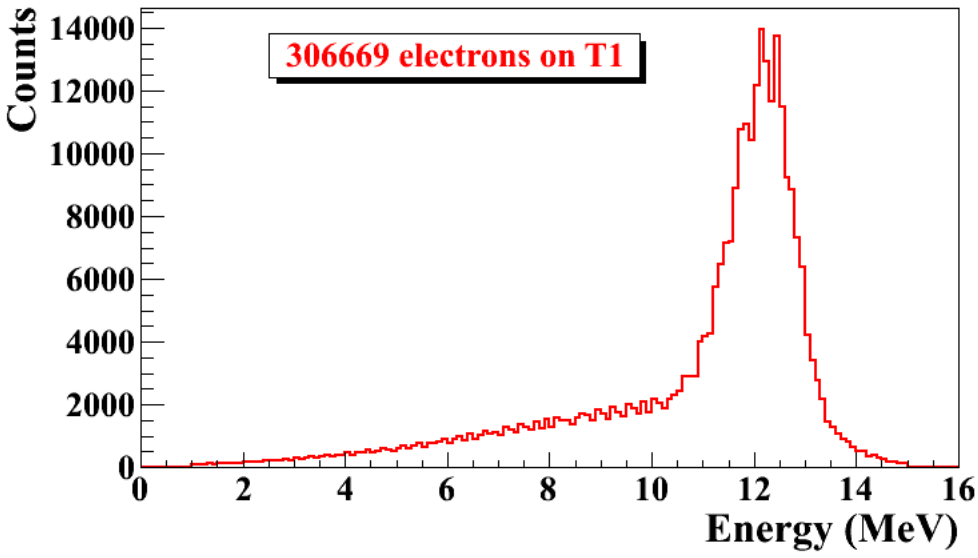

Figure 2.3: Simulated electron energy distribution right before a tungsten foil.

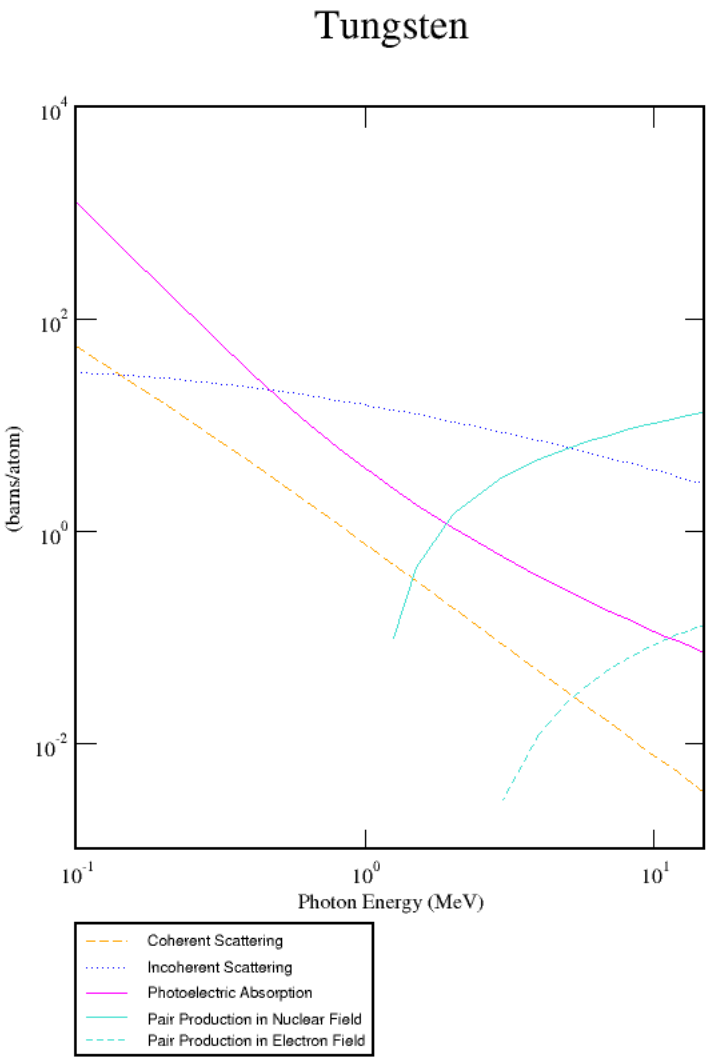

Figure 2.4: Cross section of processes that photons interacts with tungsten [7]

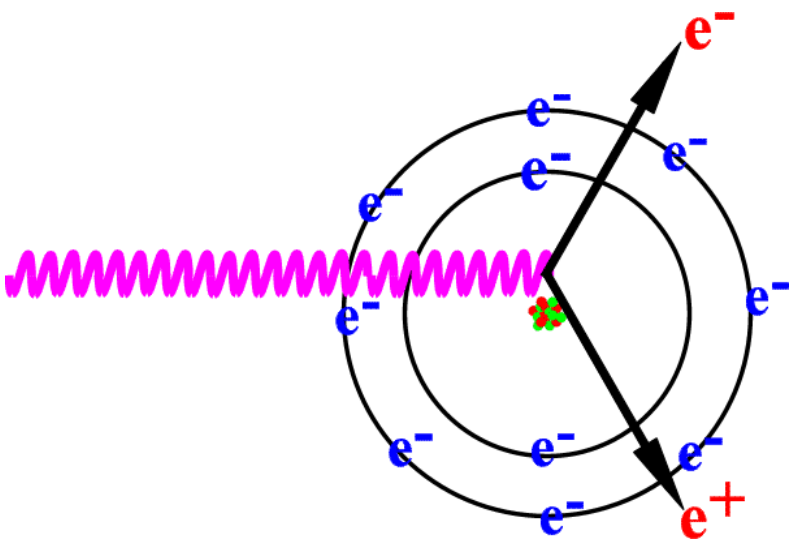

Figure 2.5: Pair production.

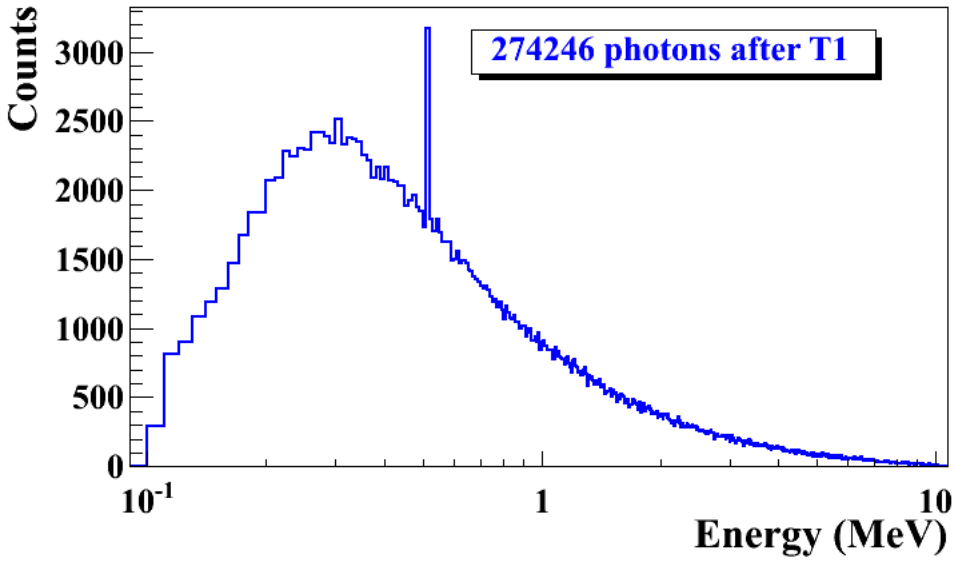

Figure 2.6: Simulated Bremsstrahlung photon energy right after a tungsten foil.

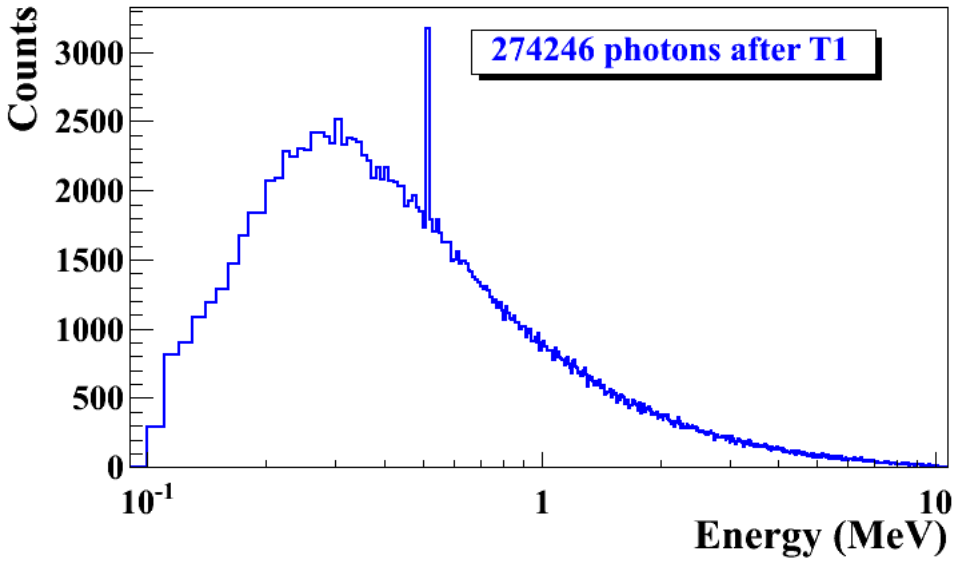

Figure 2.7: Simulated Bremsstrahlung photon energy right after a tungsten foil.

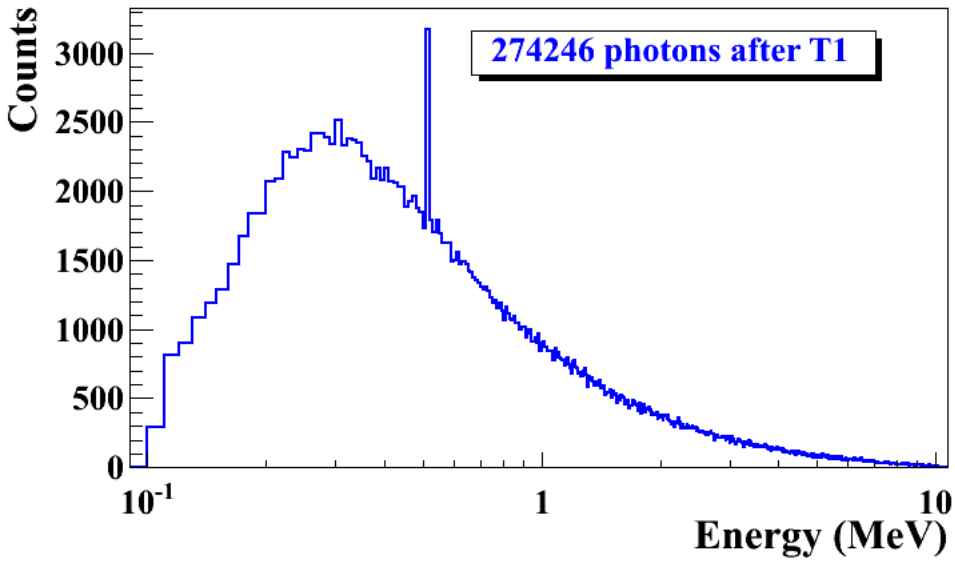

Figure 2.8: Simulated Bremsstrahlung photon energy right after a tungsten foil.

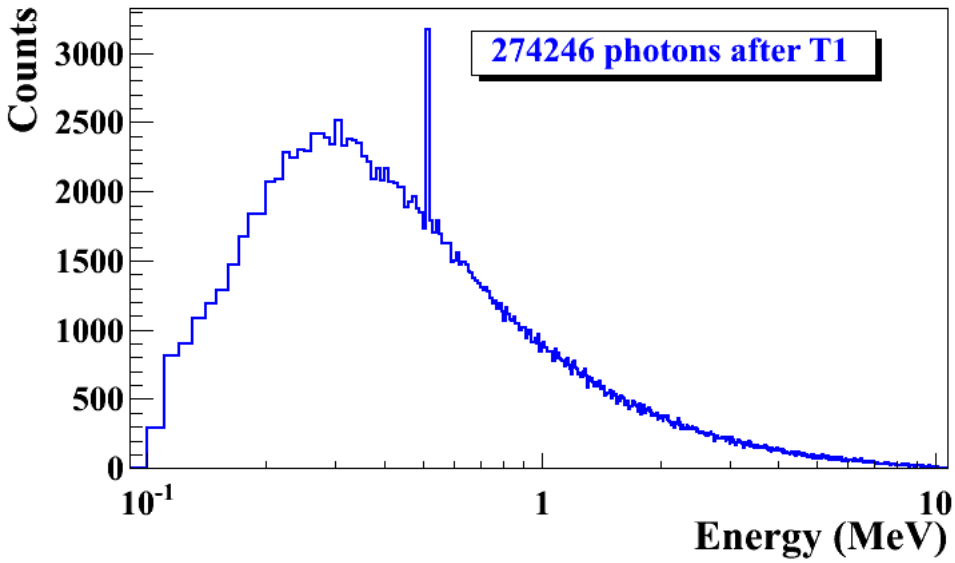

Figure 2.9: Simulated Bremsstrahlung photon energy right after a tungsten foil.

Chapter 3

Apparatus

3.1 HRRL Beamline

The first step of this experiment is to deliver an electron beam with energy around 10 MeV and with sufficient current to the tungsten foil. A 16 MeV S-band High Repetition Rate Linac (HRRL) located at the Beam Lab of the Department of the Physics, Idaho State University is used to generate incident electron beam. The energy of the HRRL can be tunable between 3 to 16 MeV and its rep and its repetition rate is tunable between 1-300 Hz. Some basic parameters of the HRRL is given in the 3.1.

Table 3.1: Emittance Measurement Results.

Parameter	Unit	Value
maximum energy	MeV	16
peak current	mA	100
repetition rate	Hz	300
absolute energy spread	MeV	2-4
macro pulse length	ns	>50

To construct a beamline can run on both positron and electron mode, the cavity is relocated to its current position and quadrupole and dipole magnets to transport the beam. As shown in Fig. 3.1 and described in Tab. 3.2 more diagnostic tools like OTR/YAG screens, Faraday cups and toroids are installed to the new beamline for diagnostic purposes of electron beam. Energy slits are added to the beamline for the control of energy/momentum spread of the beam. A insertable tungsten foil target (T1) is placed between the 1st and 2nd triplets to produce positrons when the electron beam hits it.

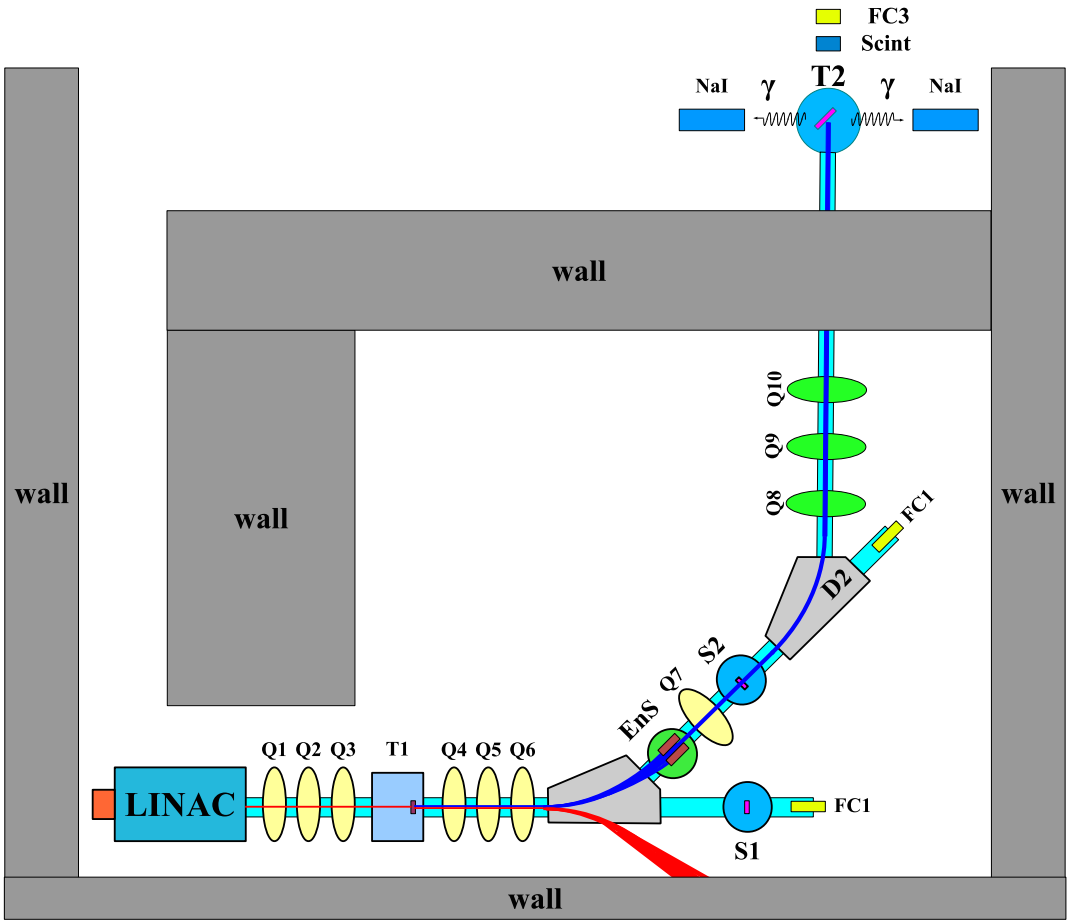

Figure 3.1: HRRL beamline layout and parts.

3.2 Electron Beam Characterization

3.2.1 Emittance Measurement

Emittance is an important parameter in accelerator physics. If emittance with twiss parameters are given at the exit of the gun, we will be able to calculate beam size and divergence any point after the exit of the gun. Knowing the beam size and beam divergence on the positron target will greatly help us study the process of creating positron. Emittance with twiss parameters are also key parameters for any accelerator simulations. Also, energy and

Table 3.2: HRRL Beamline Parts.

Label	Beamline Element
T1	positron production target
T2	positron annihilation target
Ens	energy slit
FC1, FC2	Faraday cups
Q1,..., Q10	quadrupoles
D1, D2	dipoles
NaI	NaI detectors
OTR	optical transition radiation screen
YAG	yttrium aluminium garnet screen

energy spread of the beam will be measured in the emittance measurement.

Emittance

In accelerator physics, Cartesian coordinate system was used to describe motion of the accelerated particles. Usually the z-axis of Cartesian coordinate system is set to be along the electron beam line as longitudinal beam direction. X-axis is set to be horizontal and perpendicular to the longitudinal direction, as one of the transverse beam direction. Y-axis is set to be vertical and perpendicular to the longitudinal direction, as another transverse beam direction. For the convenience of representation, we use z to represent our transverse coordinates, while discussing emittance. And we would like to express longitudinal beam direction with s. Our transverse beam profile changes along the beam line, it makes z is function of s, $z(s)$. The angle of a accelerated charge regarding the designed orbit can be defined as $z' = \frac{dz}{ds}$

If we plot z vs. z', we will get an ellipse. The area of the ellipse is an invariant, which is called Courant-Snyder invariant [8]. The transverse emittance ϵ of the beam is defined to be the area of the ellipse, which contains 90% of the particles.

Emittance Measurement

An Optical Transition Radiation (OTR) based viewer was installed to allow measurements at the high electron currents available using the HRRL. The visible light from the OTR based viewer is produced when a relativistic electron beam crosses the boundary of two mediums with different dielectric constants. Visible radiation is emitted at an angle of 90° with respect to the incident beam direction [13] when the electron beam intersects the OTR target at a 45° angle. These backward-emitted photons are observed using a digital camera and can be used to measure the shape and intensity of the electron beam based on the OTR distribution.

The emittance measurement can be performed in a several ways [9, 10]. This work used the Quadrupole scanning method [12] to measure the emittance, Twiss parameters, and beam energy.

Quadrupole Scanning Method

Fig. 3.2 illustrates the apparatus used to measure the emittance using the quadrupole scanning method. A quadrupole is positioned at the exit of the linac to focus or defocus the beam as observed on a downstream view screen. The 3.1 m distance between the quadrupole and the screen was chosen in order to minimize chromatic effects and to satisfy the thin lens approximation. Assuming the thin lens approximation, $\sqrt{k_1}L << 1$, is satisfied, the transfer matrix of a quadrupole magnet may be expressed as

$$\mathbf{Q} = \begin{pmatrix} 1 & 0 \\ -k_1 L & 1 \end{pmatrix} = \begin{pmatrix} 1 & 0 \\ -\frac{1}{f} & 1 \end{pmatrix}, \tag{3.1}$$

where k_1 is the quadrupole strength, L is the length of quadrupole, and f is the focal length. A matrix representing the drift space between the quadrupole and screen is given

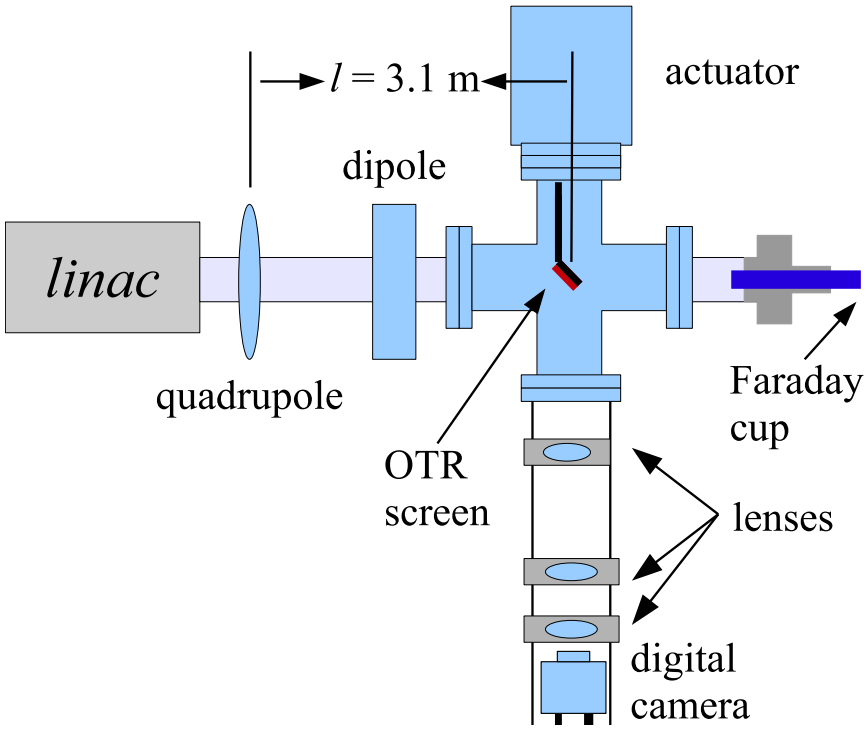

Figure 3.2: Apparatus used to measure the beam emittance.

by

$$\mathbf{S} = \begin{pmatrix} 1 & l \\ 0 & 1 \end{pmatrix}, \tag{3.2}$$

where l is the distance between the scanning quadrupole and the screen. The transfer matrix of the scanning region is given by the matrix product $\mathbf{SQ}$. In the horizontal plane, the beam matrix at the screen ($\sigma_\mathbf{s}$) is related to the beam matrix of the quadrupole ($\sigma_\mathbf{q}$) using the similarity transformation

$$\sigma_\mathbf{s} = \mathbf{M}\sigma_\mathbf{q}\mathbf{M}^\mathrm{T}. \tag{3.3}$$

where the $\sigma_{\mathbf{s}}$ and $\sigma_{\mathbf{q}}$ are defined as [11]

$$\sigma_{\mathbf{s},x} = \begin{pmatrix} \sigma_{\mathrm{s},x}^2 & \sigma_{\mathrm{s},xx'} \\ \sigma_{\mathrm{s},xx'} & \sigma_{\mathrm{s},x'}^2 \end{pmatrix},\ \sigma_{\mathbf{q},x} = \begin{pmatrix} \sigma_{\mathrm{q},x}^2 & \sigma_{\mathrm{q},xx'} \\ \sigma_{\mathrm{q},xx'} & \sigma_{\mathrm{q},x'}^2 \end{pmatrix}. \tag{3.4}$$

By defining the new parameters [12]

$$A \equiv l^2 \sigma_{\mathrm{q},x}^2,\ B \equiv \frac{1}{l} + \frac{\sigma_{\mathrm{q},xx'}}{\sigma_{\mathrm{q},x}^2},\ C \equiv l^2 \frac{\epsilon_x^2}{\sigma_{\mathrm{q},x}^2}, \tag{3.5}$$

the matrix element $\sigma_{\mathrm{s},x}^2$, the square of the rms beam size at the screen, may be expressed as a parabolic function of the product of k_1 and L

$$\sigma_{\mathrm{s},x}^2 = A(k_1 L)^2 - 2AB(k_1 L) + (C + AB^2). \tag{3.6}$$

The emittance measurement was performed by changing the quadrupole current, which changes $k_1 L$, and measuring the corresponding beam image on the view screen. The measured two-dimensional beam image was projected along the image's abscissa and ordinate axes. A Gaussian fitting function is used on each projection to determine the rms value, σ_{s} in Eq. (3.6). Measurements of σ_{s} for several quadrupole currents ($k_1 L$) is then fit using the parabolic function in Eq. (3.6) to determine the constants A, B, and C. The emittance (ϵ) and the Twiss parameters (α and β) can be found using Eq. (3.7).

$$\epsilon = \frac{\sqrt{AC}}{l^2},\ \beta = \sqrt{\frac{A}{C}},\ \alpha = \sqrt{\frac{A}{C}}(B + \frac{1}{l}). \tag{3.7}$$

3.2.2 The OTR Imaging System

The OTR target is 10 μm thick aluminum foil with a 1.25 inch diameter. The OTR is emitted in a cone shape with the maximum intensity at an angle of $1/\gamma$ with respect to the reflecting angle of the electron beam [13]. Three lenses, 2 inches in diameter, are used for the imaging system to avoid optical distortion at lower electron energies. The focal lengths

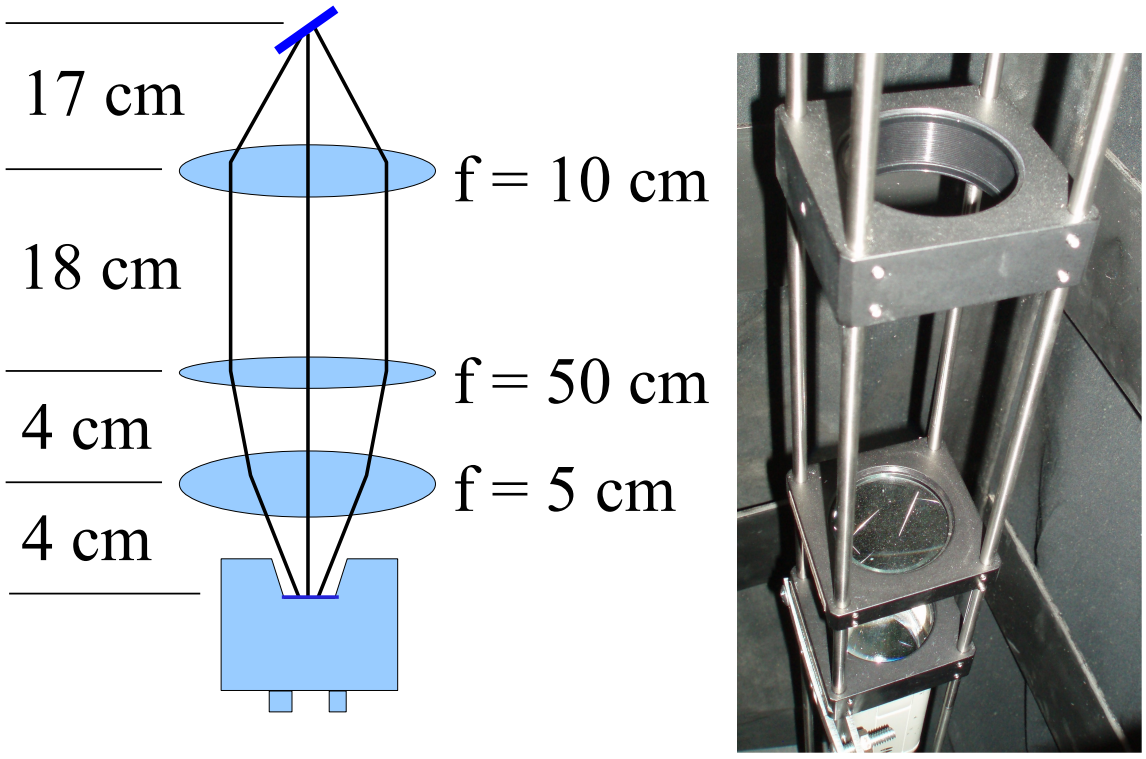

Figure 3.3: The OTR Imaging system.

and position of the lenses are shown in Fig. 3.3. The camera used was a JAI CV-A10GE digital camera with a 767 by 576 pixel area. The camera images were taken by triggering the camera synchronously with the electron gun.

Quadrupole Scanning Experiment

The quadrupole current is changed to alter the strength and direction of the quadrupole magnetic field such that a measurable change in the beam shape is seen by the OTR system. Initially, the beam was steered by the quadrupole indicating that the beam was not entering along the quadrupole's central axis. Several magnetic elements upstream of this quadrupole were adjusted to align the incident electron beam with the quadrupole's central axis. First, the beam current observed by a Faraday cup located at the end of beam line was maximized using upstream steering coils within the linac nearest the gun. Second, the first solenoid nearest the linac gun was used to focus the electron beam on the OTR

screen. Steering coils were adjusted to maximize the beam current to the Faraday cup and minimize the deflection of the beam by the solenoid first then by the quadrupole. A second solenoid and the last steering magnet, both near the exit of the linac, were used in the final step to optimize the beam spot size on the OTR target and maximize the Faraday cup current. A configuration was found that minimized the electron beam deflection when the quadrupole current was altered during the emittance measurements.

The emittance measurement was performed using an electron beam energy of 15 MeV and a 200 ns long, 40 mA, macro pulse peak current. The current in the first quadrupole after the exit of the linac was changed from $-$ 5 A to 5 A with an increment of 0.2 A. Seven measurements were taken at each current step in order to determine the average beam width and the variance. Background measurements were taken by turning the linac's electron gun off while keep the RF on. Background image and beam images before and after background subtraction are shown in Fig. 3.4. A small dark current is visible in Fig. 3.4b that is known to be generated when electrons are pulled off the cavity wall and accelerated.

The electron beam energy was measured using a dipole magnet downstream of the quadrupole used for the emittance measurements. Prior to energizing the dipole, the electron micro-pulse bunch charge passing through the dipole was measured using a Faraday cup located approximately 50 cm downstream of the OTR screen. The dipole current was adjusted until a maximum beam current was observed on another Faraday cup located just after the 45 degree exit port of the dipole. A magnetic field map of the dipole suggests that the electron beam energy was 15 $\pm$ 1.6 MeV. Future emittance measurements are planned to cover the entire energy range of the linac.

Data Analysis and Results

Images from the JAI camera were calibrated using the OTR target frame. An LED was used to illuminate the OTR aluminum frame that has a known inner diameter of 31.75 mm. Image processing software was used to inscribe a circle on the image to measure the circular OTR inner frame in units of pixels. The scaling factor can be obtained by dividing this

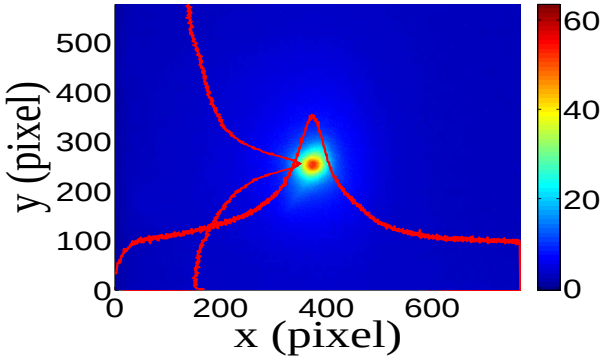

(a)

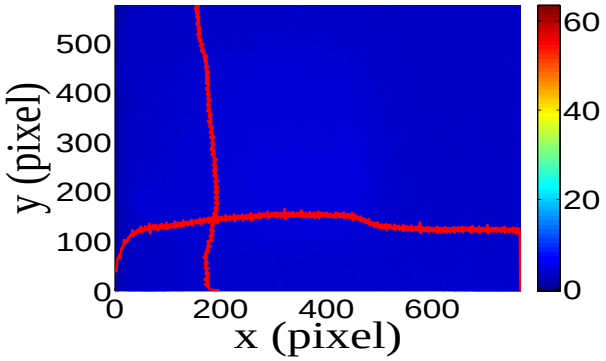

(b)

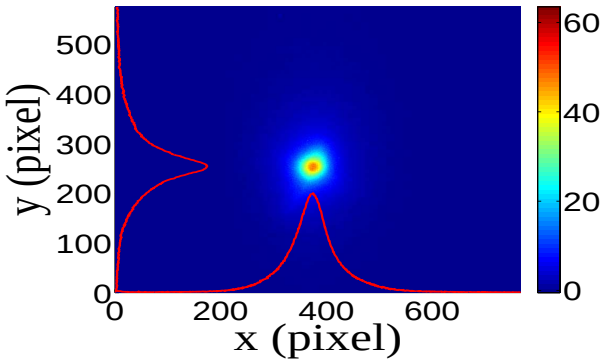

(c)

Figure 3.4: Background subtracted to minimize impact of dark current; (a) a beam with the dark current and background noise, (b) a background image, (c) a beam image when dark background was subtracted.

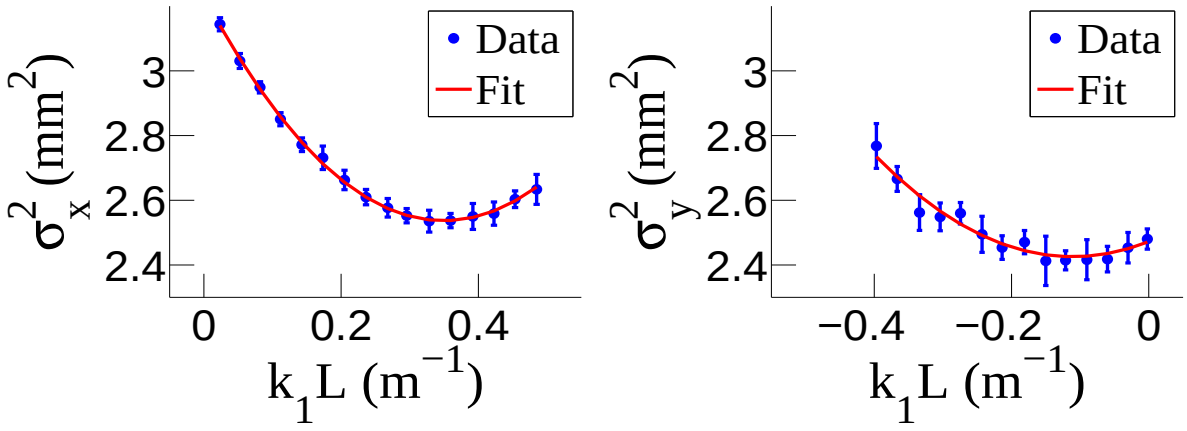

Figure 3.5: Square of rms values and parabolic fittings.

length with the number of pixels observed. The result is a horizontal scaling factor of 0.04327 ± 0.00016 mm/pixel and vertical scaling factor of 0.04204 ± 0.00018 mm/pixel. Digital images from the JAI camera were extracted in a matrix format in order to take projections on both axes and perform a Gaussian fit. The observed image profiles were not well described by a single Gaussian distribution. The profiles may be described using a Lorentzian distribution, however, the rms of the Lorentzian function is not defined. The super Gaussian distribution seems to be the best option [14], because rms values may be directly extracted.

Fig. 3.5 shows the square of the rms (σ_s^2) *vs* k_1L for x (horizontal) and y (vertical) beam projections along with the parabolic fits using Eq. 3.5. The emittances and Twiss parameters from these fits are summarized in Table 3.3. An automatic MATLAB based emittance measurement tool is under development.

3.2.3 Conclusions

A diagnostic tool was developed and used to measure the beam emittance of the High Rep Rate Linac at the Idaho Accelerator Center. The tool relied on measuring the images generated by the optical transition radiation of the electron beam on a polished thin aluminum target. The electron beam profile was not described well using a single Gaus-

Table 3.3: Emittance Measurement Results.

Parameter	Unit	Value
projected emittance ϵ_x	μm	0.37 ± 0.02
projected emittance ϵ_y	μm	0.30 ± 0.04
β_x-function	m	1.40 ± 0.06
β_y-function	m	1.17 ± 0.13
α_x-function	rad	0.97 ± 0.06
α_y-function	rad	0.24 ± 0.07
micro-pulse charge	pC	11
micro-pulse length	ps	35
energy of the beam E	MeV	15 ± 1.6
relative energy spread $\Delta E/E$	%	10.4

sian distribution but rather by a super Gaussian or Lorentzian distribution. The larger uncertainties observed for σ_y^2 are still under investigation. The projected emittance of the High Repetition Rate Linac, similar to medical linacs, at ISU was measured to be less than 0.4 μm as measured by the OTR based tool described above when accelerating electrons to an energy of 15 MeV. The normalized emittance may be obtained by multiplying the projected emittance by the average relativistic factor γ and β of the electron beam. We plan to perform similar measurements over the energy range of the linac in the near future.

3.3 Energy Scan

Energy scan was done to measure the energy profile of HRRL at nominal 12 MeV. A Faraday cup was placed at the end of the 45 degree beamline to measure the electron beam current bent by the first dipole. Dipole coil current were changed by 1 A increment and the Faraday cup currents were recorded. The scan results with corresponding beam energies are shown in the table below. The relation between dipole current and beam energy is given in the appendix. The energy distribution of HRRL can be described by two skewed Gaussian fit overlapping [14]. The measurement result and fit are shown in Fig. 3.6 and in Table 3.4

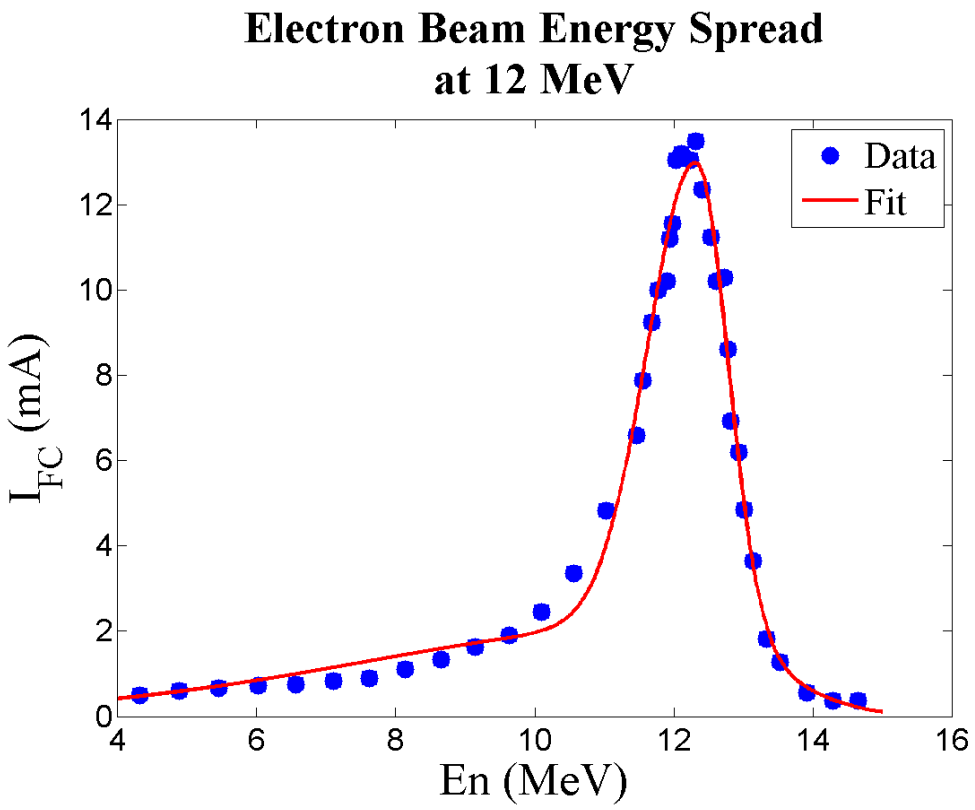

Figure 3.6: HRRL energy scan (blue dots) and fit (red line).

3.4 Positron Detection

Positron Detection section setup is shown in Fig. 3.7

3.4.1 NaI Detectors

NaI crystals, shown as in Fig. 3.9, acquired from IAC were used to detect 511 keV photons from positron annihilation. Since the detectors had pulse length around 400 μs, the PMT bases were redesigned and rebuilt. The NaI detectors have two outputs, one is at second last dynode and one anode signal. PMT base configuration of the NaI detectors is shown in the Fig. 3.8 and bases made shown in Fig. 3.10. It takes ADC 5.7 μs to convert analog signal to digital signal. The signal from anode was delayed 6 μs by long cable and sent to the ADC. PMT base take HV around -1150 V.

Table 3.4: Emittance Measurement Results.

Parameter	First Gaussian	Second Gaussian
A amplitude	2.14	10.88
μ mean (MeV)	12.07	12.32
σ_L sigma left (MeV)	4.47	0.70
σ_R sigma right (MeV)	1.20	0.45

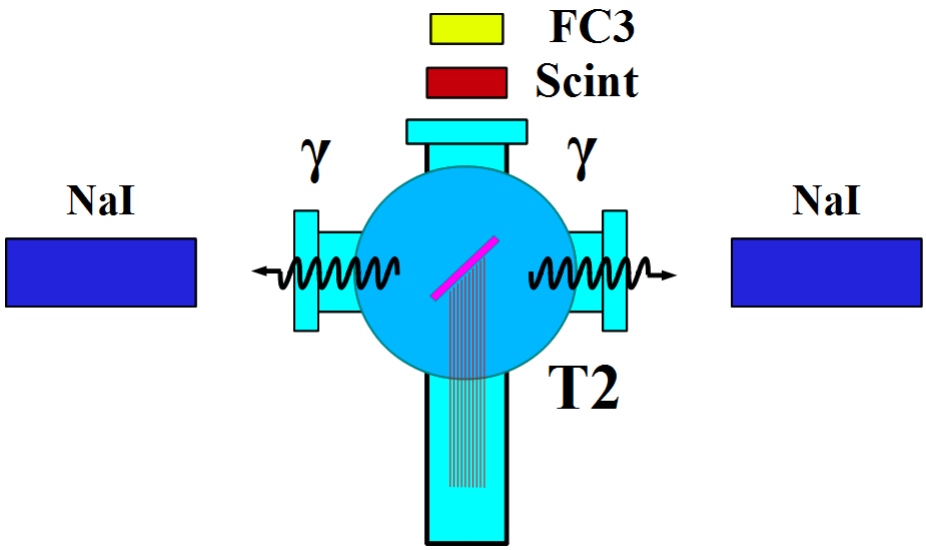

Figure 3.7: Positron Detection.

Rebuilt PMT bases: oldbase pulse length 400 s. new base pulse length 1 s.

The NaI crystal is SAINT-GOBAIN CRYSTAL & DETECTORS (MOD. 3M3/3) with sizes of 3x3.

Co60: 1173 keV and 1332 keV Na22: 1275 keV and 511 keV

3.4.2 Trigger for DAQ

The trigger for DAQ required a coincidence between one or more NaI detectors and the electron accelerator gun pulse. The last dynode signals from left and right NaI detectors were inverted using a Ortec 474 amplifier and sent to a Constant Fraction Discriminator (CFD Model specs). RF noise from the accelerator is as large as the signal from the NaI

detector. Since it is correlated in time with the gun pulse, the gun pulse was used to generate a VETO pulse that prevent the CFD from triggering on this RF noise. After this discrimination and RF noise rejection, the discriminated dynode signals were sent to an Octalgate Generator (Model) that increased the width of the logic signals to prevent multiple pulses during a single electron pulse. Then the signals were sent to Quad Coincidence to generate AND logic between electron gun and dynode signals. The logic is set as:

$$(NaI\ Left\ \&\&\ Gun\ Trigger)\ \&\&\ (NaI\ Rgiht\ \&\&\ Gun\ Trigger). \tag{3.8}$$

This is to make sure we have trigger when photons back to back scatter to the NaI detectors when electron gun is on. Then this trigger was sent to ORTEC Gate & Delay Generator. One of the out from gate generator was used to generate a gate to read analog signal from anode. Another output was delayed by 6 s, necessary time to convert the analog signal from anode to digital signal, and used as trigger for the DAQ.

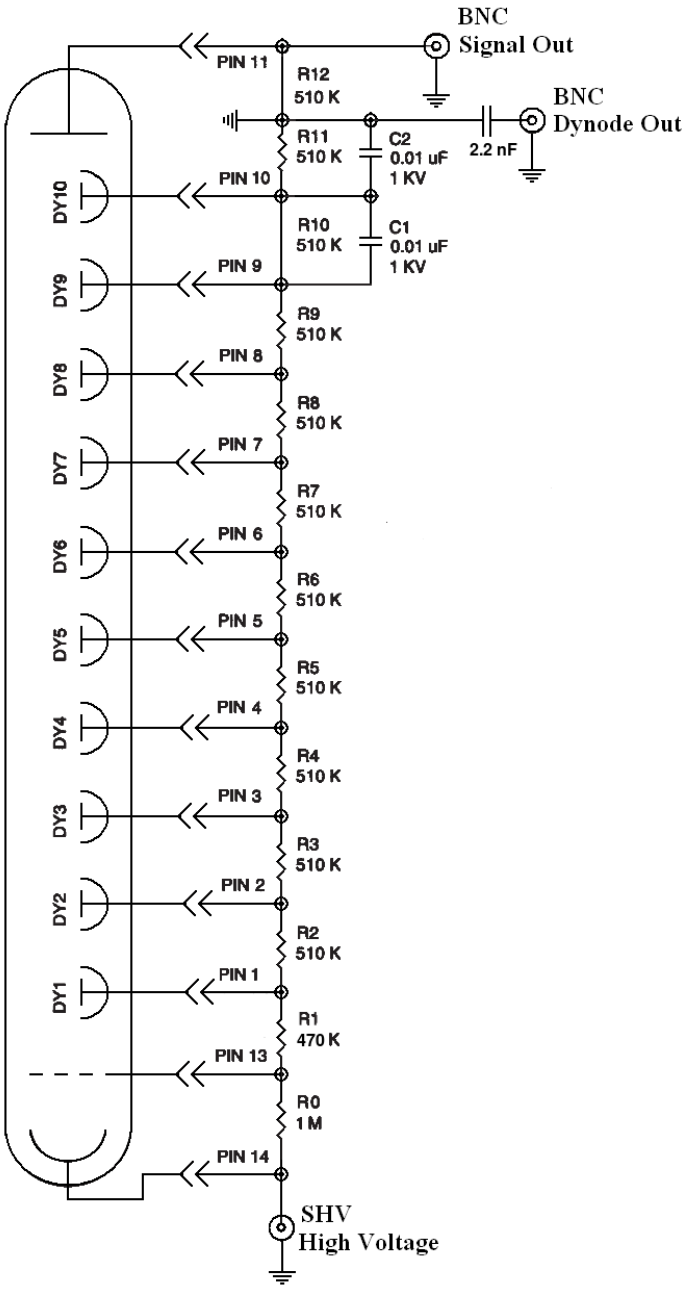

Figure 3.8: Modified PMT base design.

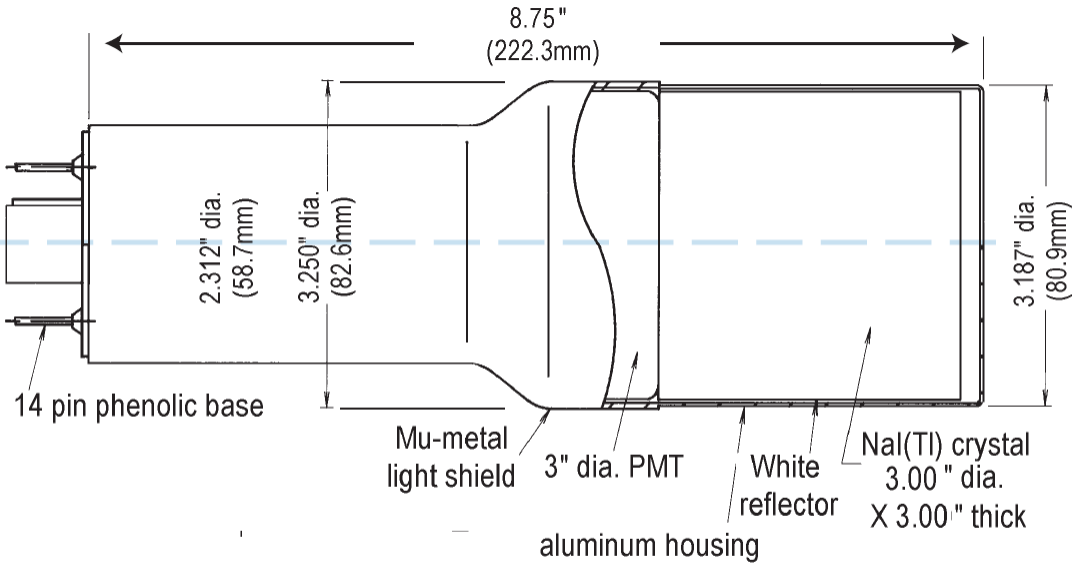

Figure 3.9: NaI crystal dimension.

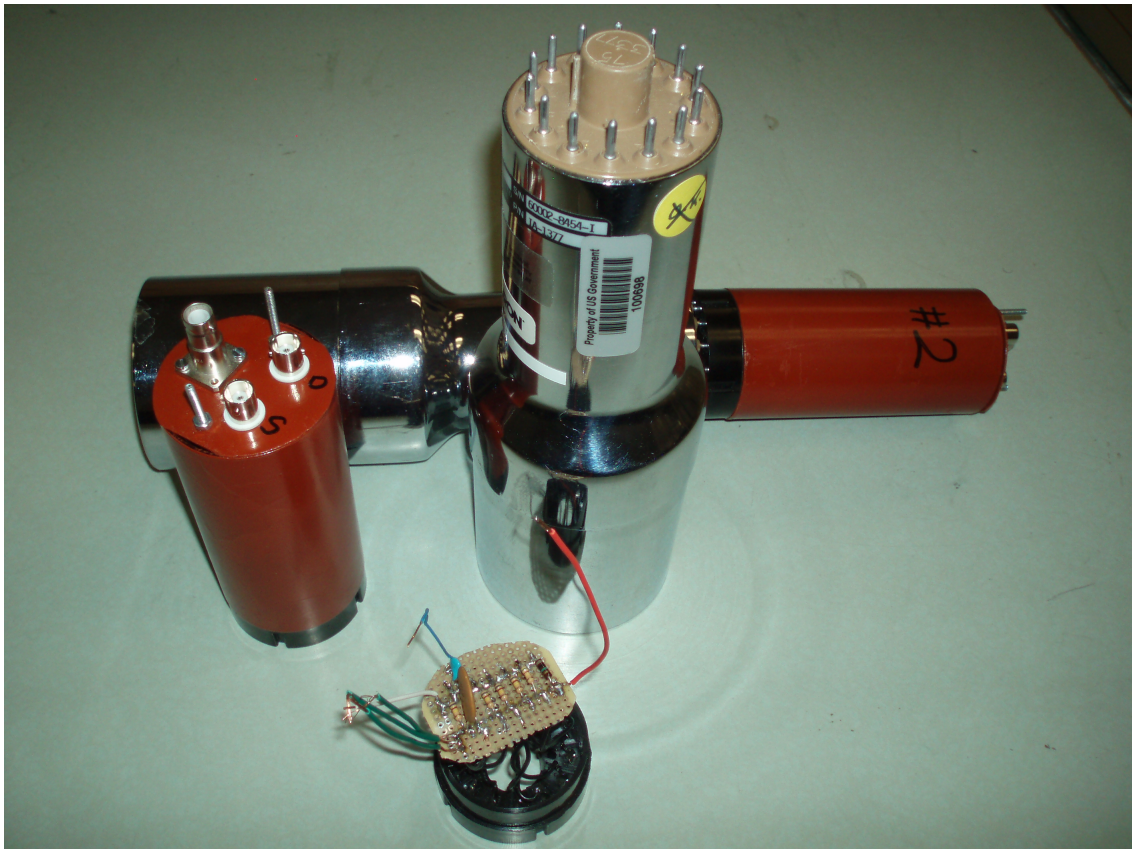

Figure 3.10: NaI crystals and new bases.

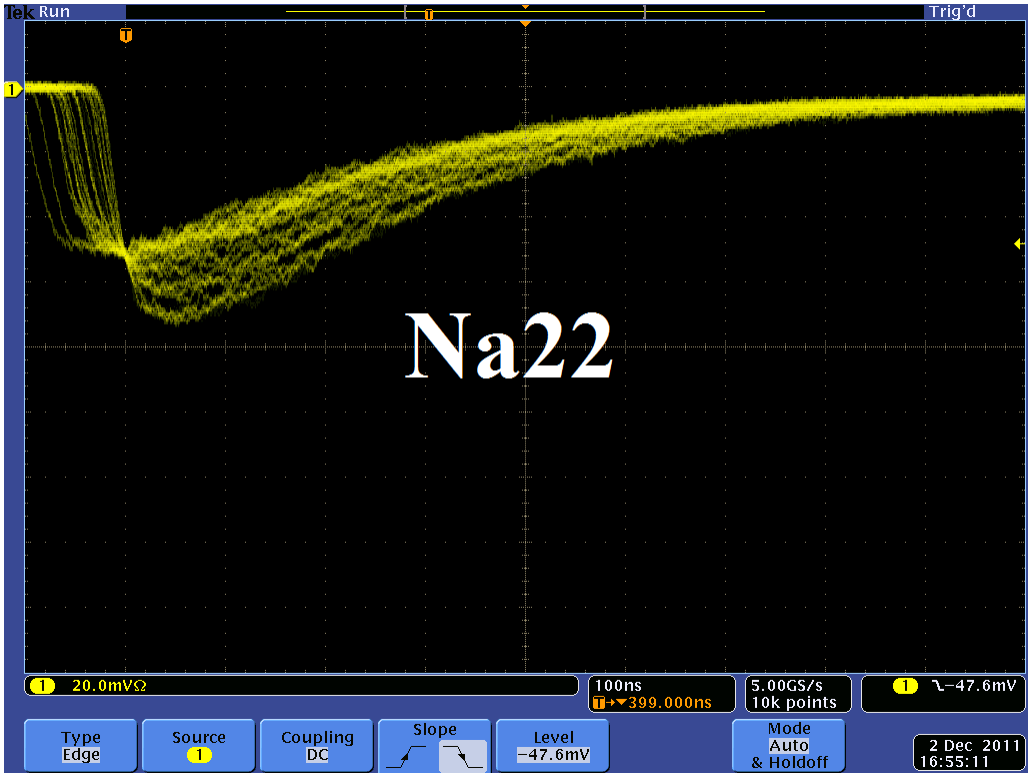

Figure 3.11: Pulses from Na22 source observed on the scope.

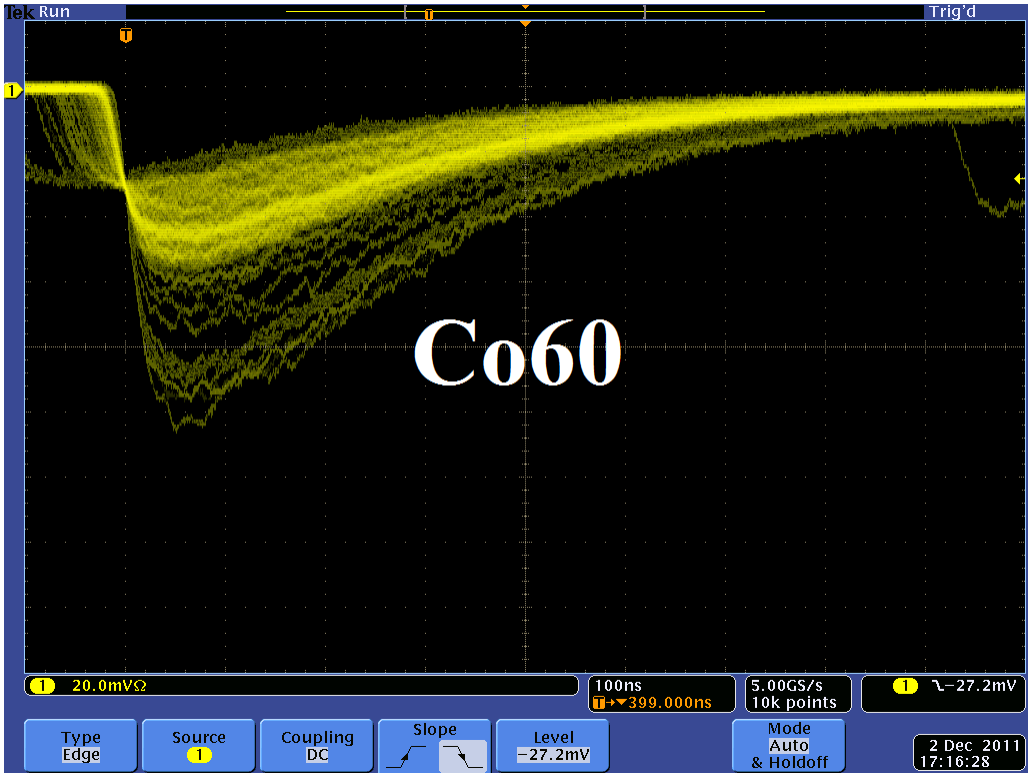

Figure 3.12: Pulses from Co60 source observed on the scope.

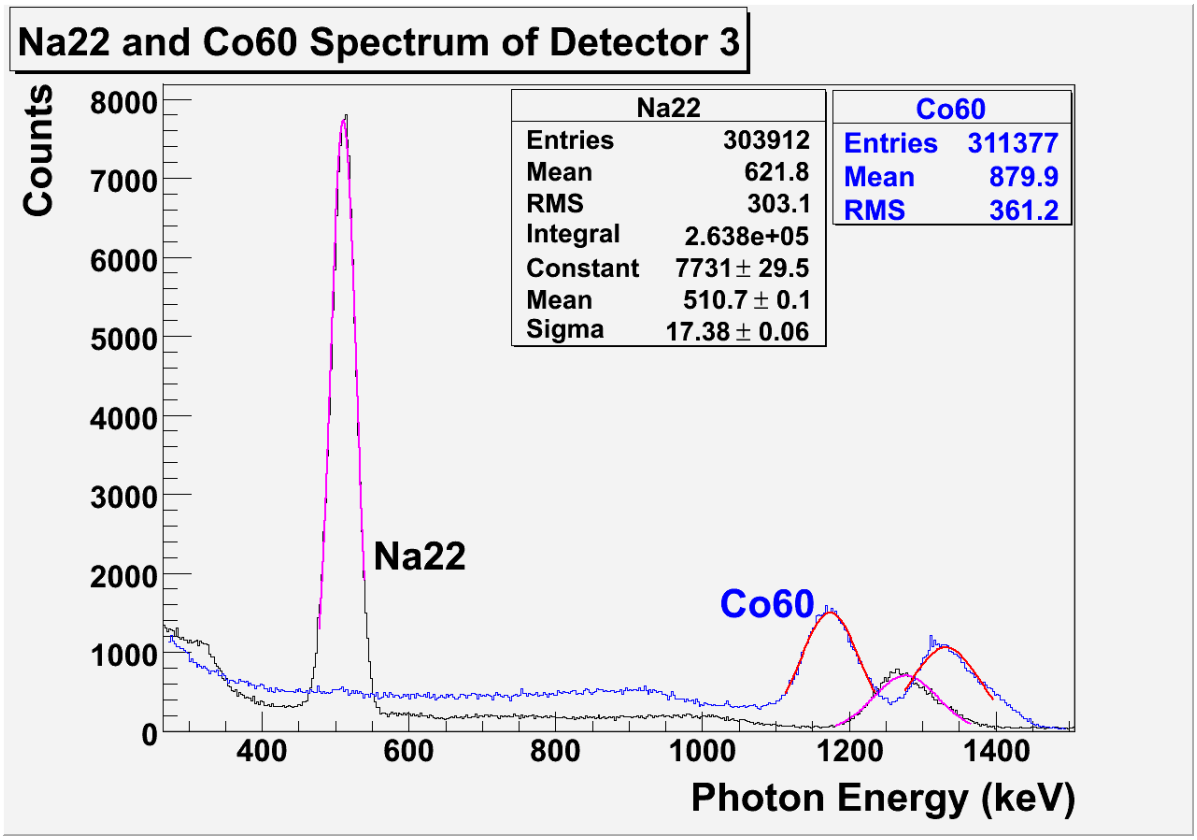

Figure 3.13: Calibrated NaI spectrum of with sources.

Chapter 4

Experiment

4.1 Runs

The annihilation target T2 is can be inserted or removed from the center of the beamline. This allow two kind runs, T2 in and T2 out. When T2 is in the positions are delivered to T2 and thermalize and annihilate produces 511 KeV photons. This photons are detected by the NaI detectors as shown in Fig. 4.1. When T2 is out, positrons exits beamlien and transported to the beam dump. NaI detectors are shielded with Pb bricks from the beam dump. T2 out runs serve as background measurements.

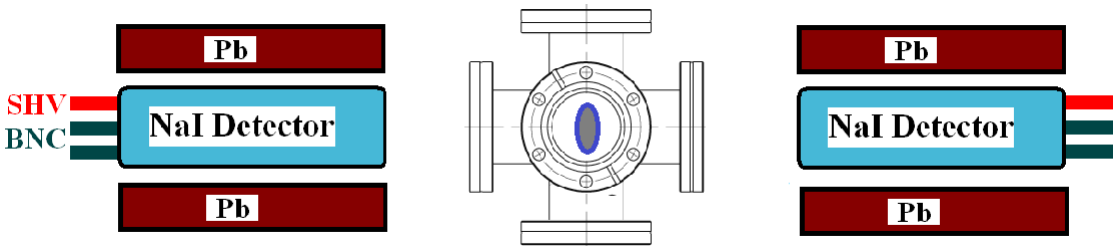

Figure 4.1: Positron detection using T2 and NaI detectors.

T2 is placed inside a 6-way cross and two horizontal side it sealed with thin windows. Two NaI detectors placed horizontally to T2, perpendicular to the 90 degree beamline and pointed to this windows.

4.2 Signal Extraction

For 3 MeV and on detector show all the steps 1. Raw counts target in and out (calibrated energy) 2. Normalized counts 3. background subtracted 4. Integral (zoomed in and with

Table 4.1: Run 3735

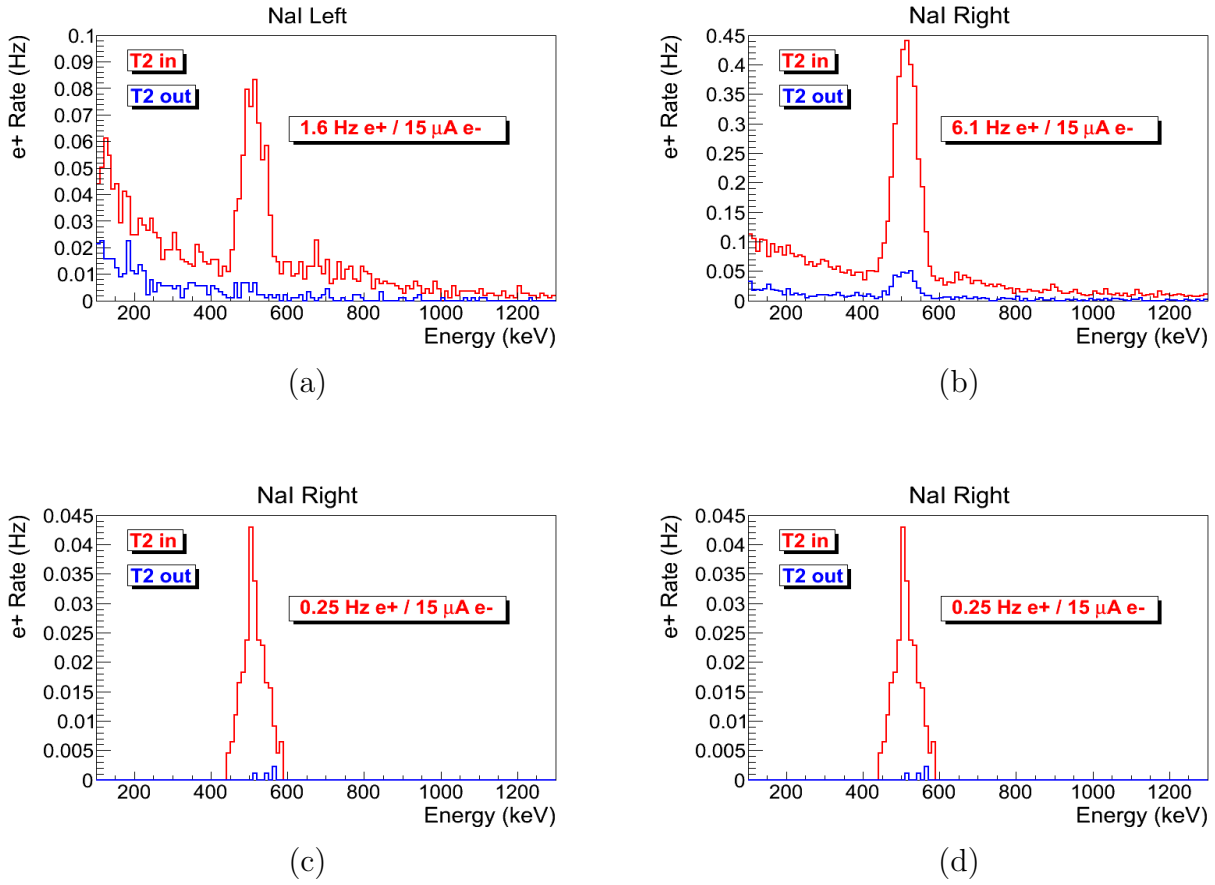

Table 4.2: Top row: original spectrum. Bottom row: incidents only happens around 511 keV peak and on both detectors.

error) Example of error propagation for the above

Raw counts target in and out Lets take example of run#3735 for the data analysis. The integral shown in red is from the background is subtracted spectrum.

4.3 Electron Current Estimation

A photon scintillator was placed between quadrupole 9 and quarupole 10 shown as in the Fig. 4.2 and used as electron beam monitor. To calibrate this scintillator electron beam

Table 4.3: Run 3735

Parameter	Unit	Value
run number		3735
reprate	Hz	300
run time	s	1002
Pulses		301462
Events		9045
e+ Counts NaI Detectors		256 ± 16

changed incrementally and the charge was measured both on oscilloscope and ADC. As the electron beam increases the beam charge observed on the scope increased and the photon peak in the ADC also shifted towards right end of the spectrum. The result shows that the relation between electron beam current and scintillator ADC channel number is linear, $(0.93 \pm 0.14)/50$ nVs/(ADC channel). The spectrum taken is shown in Fig 4.3.

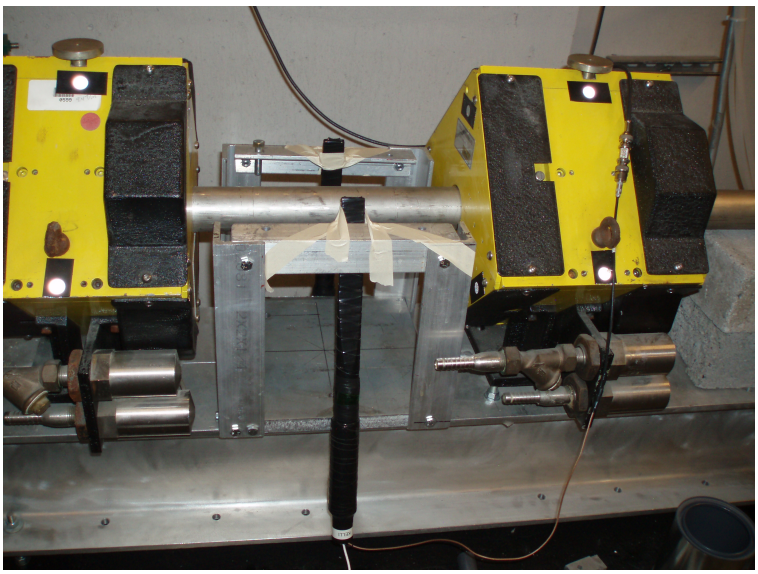

Figure 4.2: Electron beam monitor.

To find the average charge in a run two methods were used. One method calculates charge bin by bin.

$\sum_i i \times (bin\ content[i]) \times Q_{Calb} \times (pulses/events)$.

Another method uses the mean of the of the spectrum, multiply it with total number

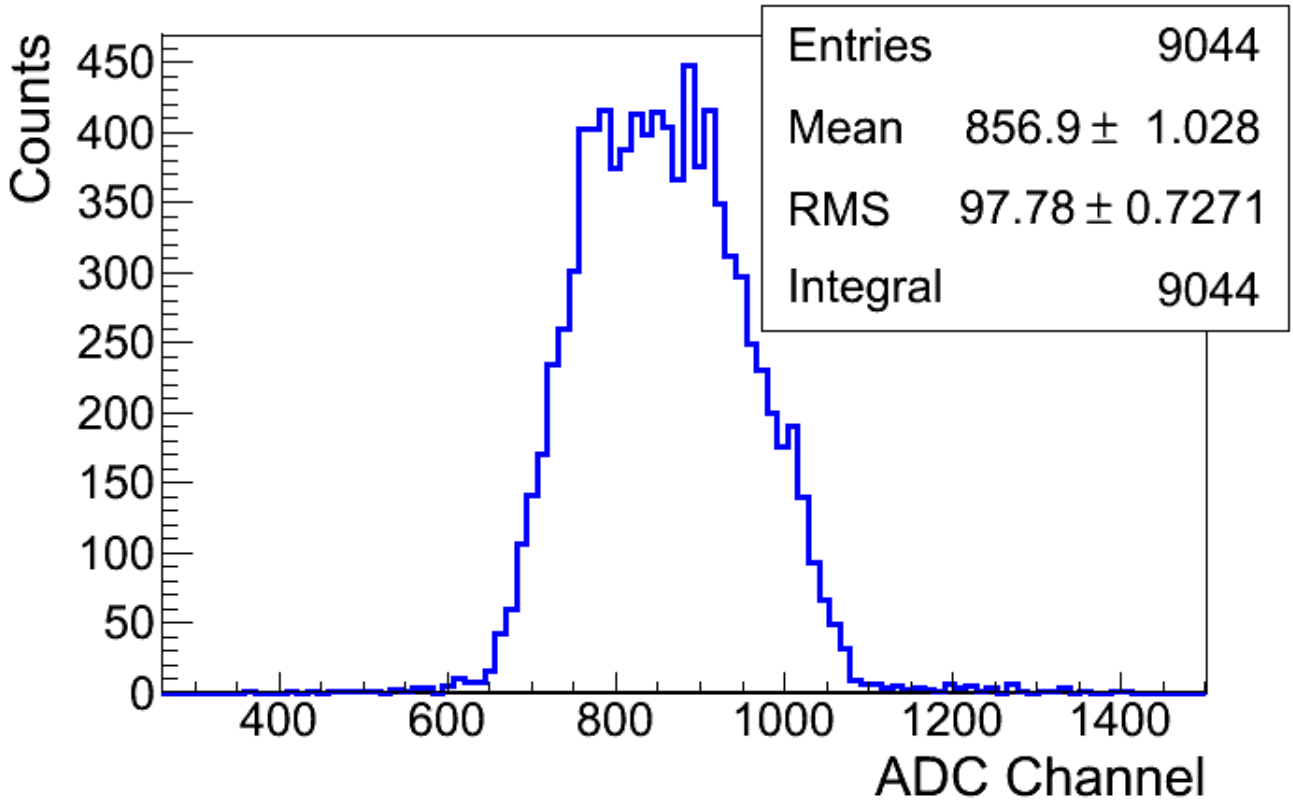

Figure 4.3: Electron beam monitor ADC signal

of pulses and the multiplies it with calibration factor. The average of the two methods is taken.

For example, the electron rate calculation in run 3735 is calculated as following.

$\sum_i i \times (bin\ content[i]) \times (856.9 \pm 1.0)(ADC\ channel) \times (301462/9045) = (4.8 \pm 0.7) \times 10^{-3}\ C$.

Total charge of electrons in this run with method 2 is

$Q_{e^-} = (856.9 \pm 1.0)(ADC\ channel) \times 301462 \times (0.93 \pm 0.14)/50(nVs/(ADC\ channel)) = (4.8 \pm 0.7) \times 10^{-3}\ C$.

The average of the two is$(4.8 \pm 0.5) \times 10^{-3}\ C$.. Then this total charge can be used to calculate total numbers of the electrons or average current of electron beam in this run.

4.4 Positron Current Estimation

Fig. 4.4 are the background subtracted spectrum. The (a) and (b) are NaI left and right detectors' spectrum. The (c) and (d) are NaI left and right detectors' spectrum with cut around 511 keV peak and after requiring coincident event on both detectors.

Table 4.4: Run 3735

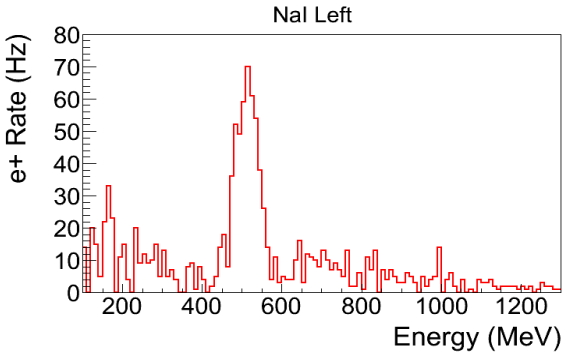

(a) Left NaI

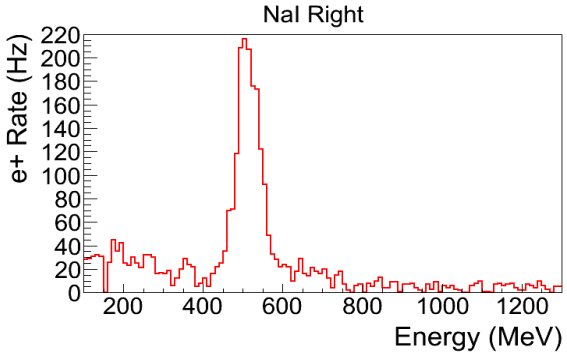

(b) Right NaI

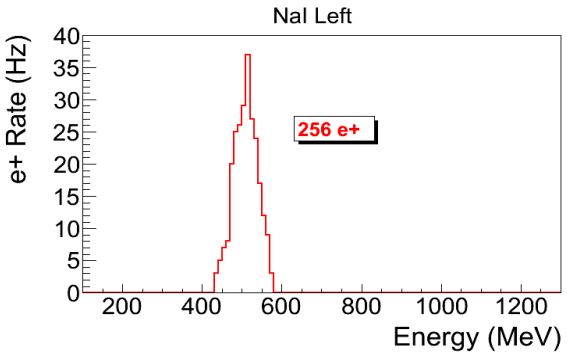

(c) Left NaI with cut and coincidence

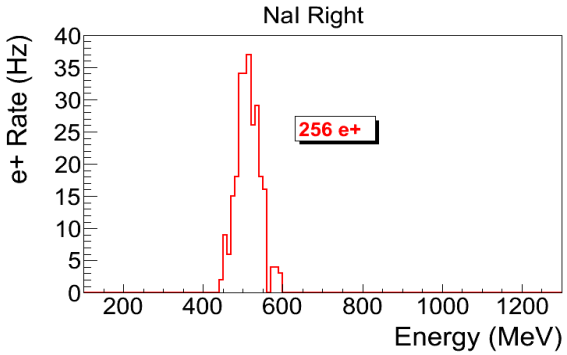

(d) Right NaI with cut and coincidence

Table 4.5: NaI positron run spectrum.

4.4.1 Positron to Electron Ratio

The measured ratio of positron to electron ratio is given the following Table 4.6 and Fig. 4.4.

Table 4.6: Run 3735

Energy	Positron to Electron Ratio
1.03 ± 0.13	0.19 ± 0.19
2.15 ± 0.13	0.69 ± 0.24
3.0 ± 0.13	8.25 ± 0.96
4.02 ± 0.13	4.20 ± 0.80
5.0 ± 0.13	0.62 ± 0.16

4.4.2 Sources of Systematic Errors

Error on Energy

To find Error on the energy, the electron beam is directed to the phosphorous screen at the end of the 90 degree beamline. The beam centered then steering away from the center. The current change on the dipole I when beam is center and at the edge is 0.2 A. This is corresponding to 0.13 MeV in beam energy.

Error on Ratio

Error on electron beam is derived from:

Error on positron beam rate is derived from: $\sqrt{\frac{positron\ rate}{run\ time}}$

Annihilation target angle

Use simulation to determine how sensitive annihilation of positrons is to angle.

What is the dependence of the annihilation target angle with the probability of a positron annihilating in the target and producing a photon that is detected by the NaI detector,

What is the distribution of 511s as a function of angle phi when theta is 90 degrees? Are they uniformly produced?

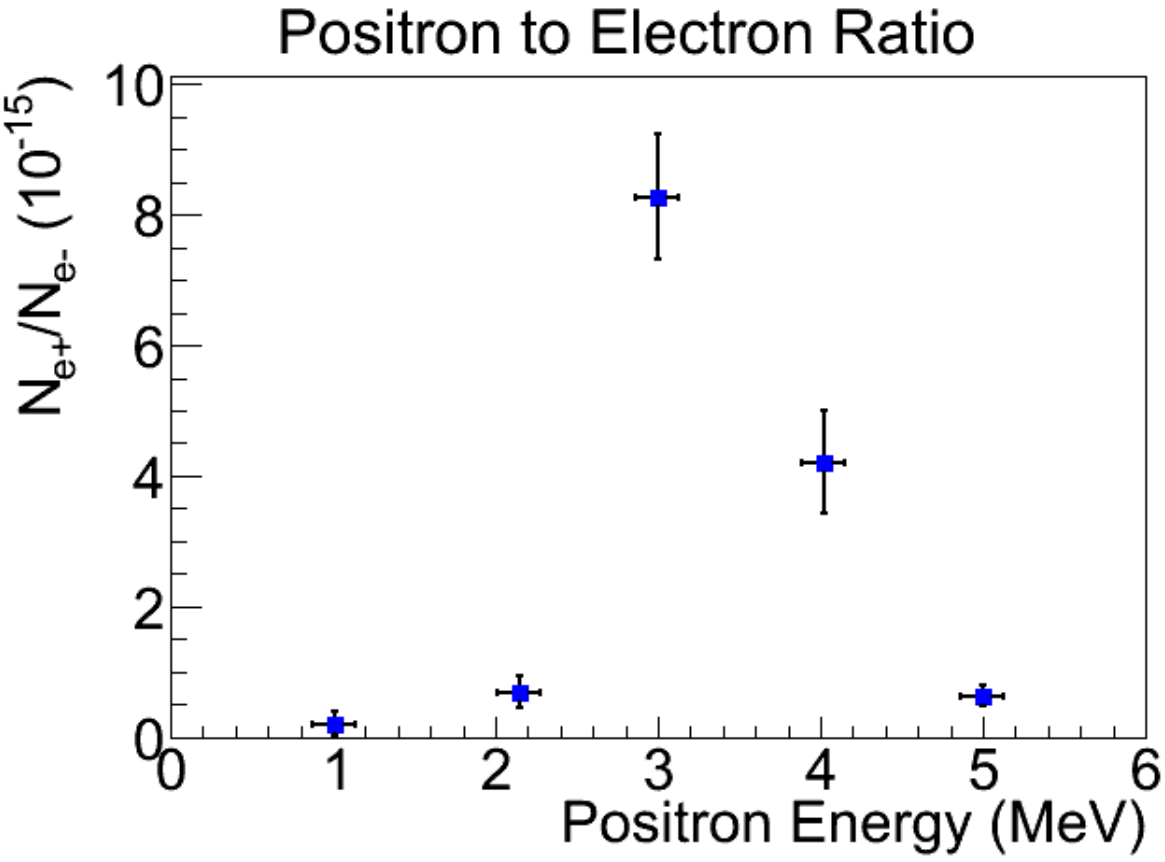

Figure 4.4: Left NaI

Energy cut systematics

How does the positron production efficiency change when you change the range of the 511 cut.

Chapter 5

Simulation

A simulation was performed using the package G4beamline(ref Muons inc) to study the processes of position generation and transportation. "G4beamline is a particle tracking and simulation program based on the Geant4 (refernce G4) toolkit that is specifically designed to easily simulate beamlines and other systems using single-particle tracking." Since the ratio of e+/e- during the positron generation process is very low (on the order of 0.001) and the positron beam loss during the transportation is large, it was necessary to divide whole process into 5 steps. A new beam event generator is created based on the results of the previous step in the simulation. The first step generates electrons according to a measurement made of the accelerator that was used in the experiment. Electrons are transported to T1 in vacuum and as a result the interactions of the electron with T1 produce positrons. The second step is the transportation of the positrons generated at T1 to the entrance of first dipole magnet. The third step is the transportation of the positrons from the entrance of the first dipole magnet to the end of the second dipole. The fourth step is the transportation of the beam from the exit of the second dipole to the T2 target. The fifth step is the positron beam interaction with T2 and detection of the resulting 511 keV photons.

5.1 Step 1 - The Electron Beam Generation and Transpiration to T1

In this step, an electron beam is generated from the experimental measure electron beam parameters. The Twis parameters described in the earlier chapter used electron generated the beam. The energy distribution is of the beam is measured and shown in the Fig. 3.6. The blue dots are measurements and red line are the fit composed of two skewed Gaussian distributions. The fit parameters are given in the Table 3.4

Series of virtual detectors are placed along the beamline to sample the beam. As an example, in the Fig. 5.1 shown are three detectors and the T1. The electron beam is observed at DUPT1 (Detector 25.52 mm UPstram of T1) and positrons (or electrons and photons) generated during the interaction of electron beam with T1 are observed at DT1 (Detector of T1) and DDNT1 (Detector DowN 25.52 mm stream of T1). In the Fig. **??**, the incoming electron beam (observed at DUPT1) energy distribution (red) and positrons generated by this electron beam (observed at DDNT1) is shown in blue.

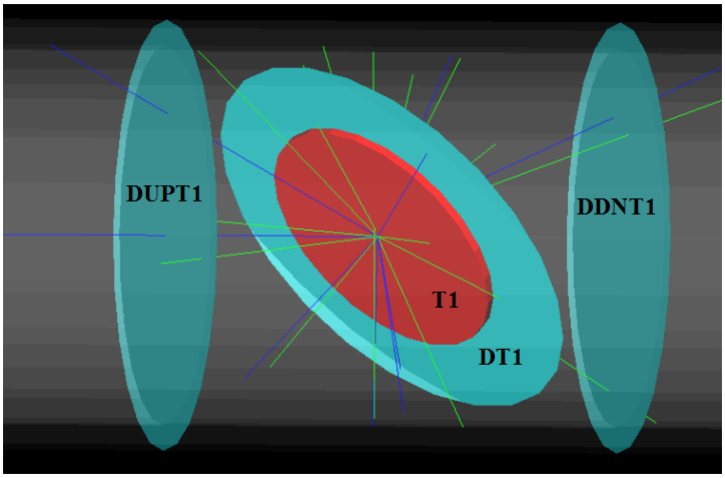

Figure 5.1: T1: Positron production target; DUPT1: upstream detector; DDNT1: down stream (DDNT1); DT1: detector right after T1.

5.1.1 Positron Beam on DDNT1

13,799,743,900 electrons were shot on T1 and resulted positron beam observed at DDNT1 is as shown below Figures.

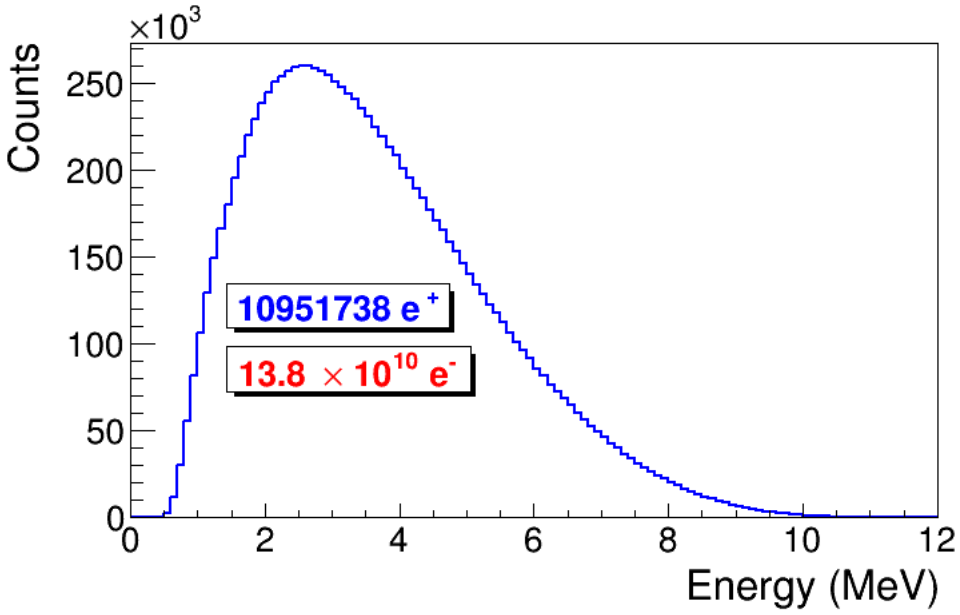

Figure 5.2: En DDNT1 e+

The Y-position distribution of the beam shown in Fig. 5.7 (Fig. 5.8 is zoomed in of Fig. 5.7.) has a sharp drop in the region between -25.8 mm and -27.2 mm that corresponds to the boundary of the target T1. Fig. 5.9 shows the geometry of the target T1 and the sensitive detector DDNT1. If the target size was increased, it would eventually intersected the detector DDNT1 at a distance of 25.8 mm from the beam center. A 1.4 mm wide stripe of low counts is visible on DDNT1 that is a result of the target's thickness of 1.016 mm and the 45 degree angle of intersection ($1.016\sqrt{2} = 1.44$). The edge of the target does not produce many positrons compared to the face of the target, and as a result you see the stripe.

As shown in Figs. 5.10 and 5.11 (zoomed figure) the positron distribution decrease occures at = 45o. Positrons are emitted from both the downstream and upstream side of the target. As shown in the figure, positrons from the downstream side of the target

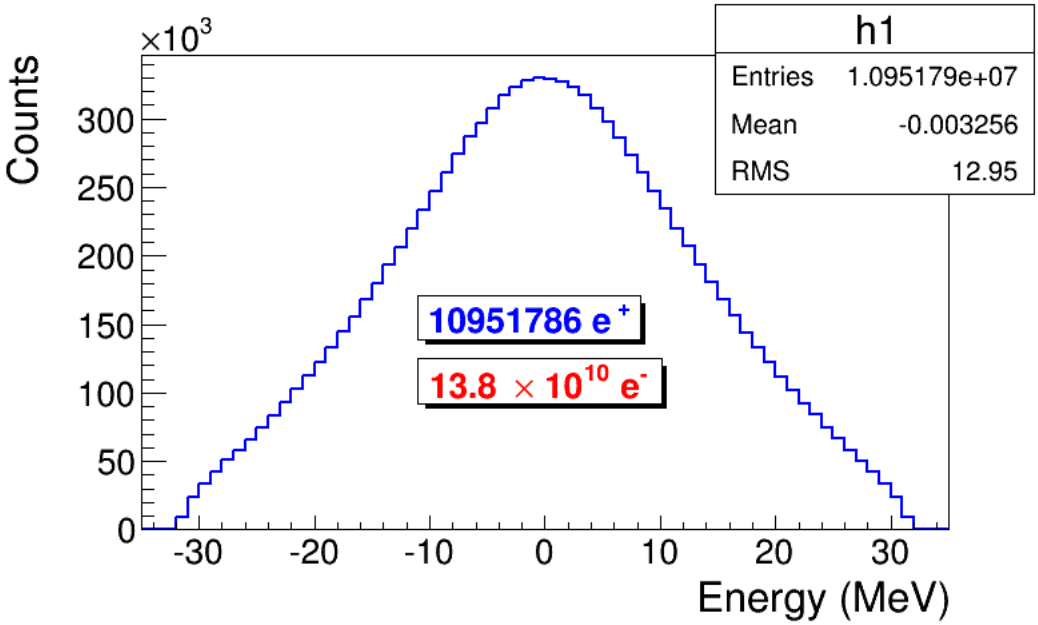

Figure 5.3: X DDNT1

intersect the detector at angles below 45 degrees while positrons from the upstream side of the target begin to hit the detector at angles beyond 45 degrees. The 1.4 mm gap represents the transition of positrons between these two extremes.

5.1.2 Positron Beam on DQ4 and DD1

Resulted positron beam on DQ1 and DD1 are shown in below Figures.

5.2 Step 2 - Transportation of the The Positron Beam after T1 to The Entrance of The First Dipole

In this step, the positrons generated in the first step divided into 1 keV/c momentum bins and each bin is sampled individually since the momentum of the positrons related to their divergence. Multiple beams with individual weights generated at downstream T1 detector DDNT1 and transported to entrance of the D1. Virtual detectors are placed at the entrance

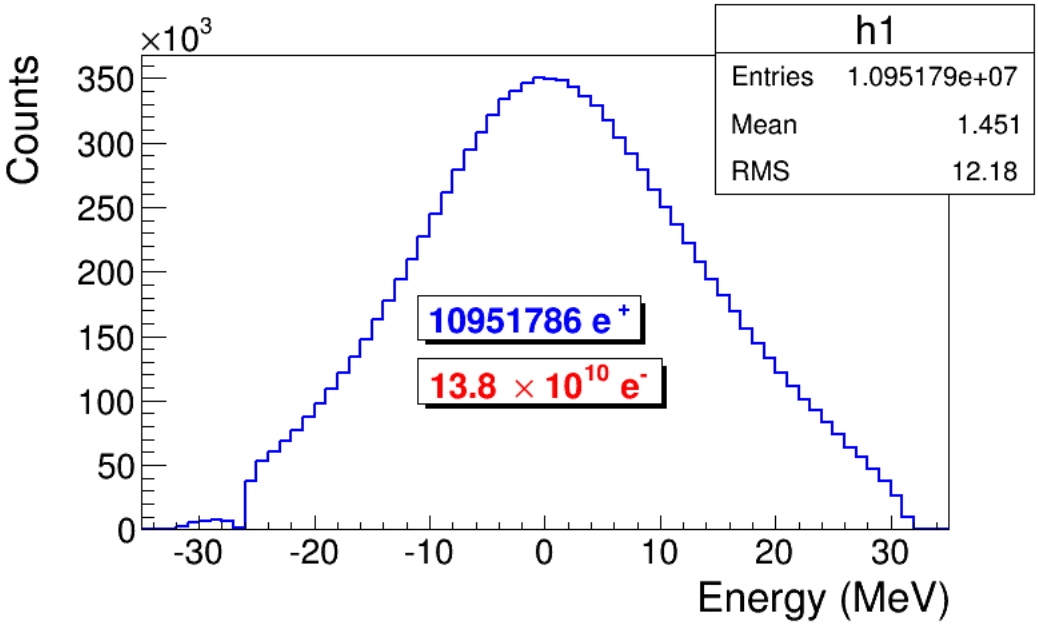

Figure 5.4: Y DDNT1

of Q4 and entrance of D1 to track positrons and generate beam for next step as shown in the Fig **??**.

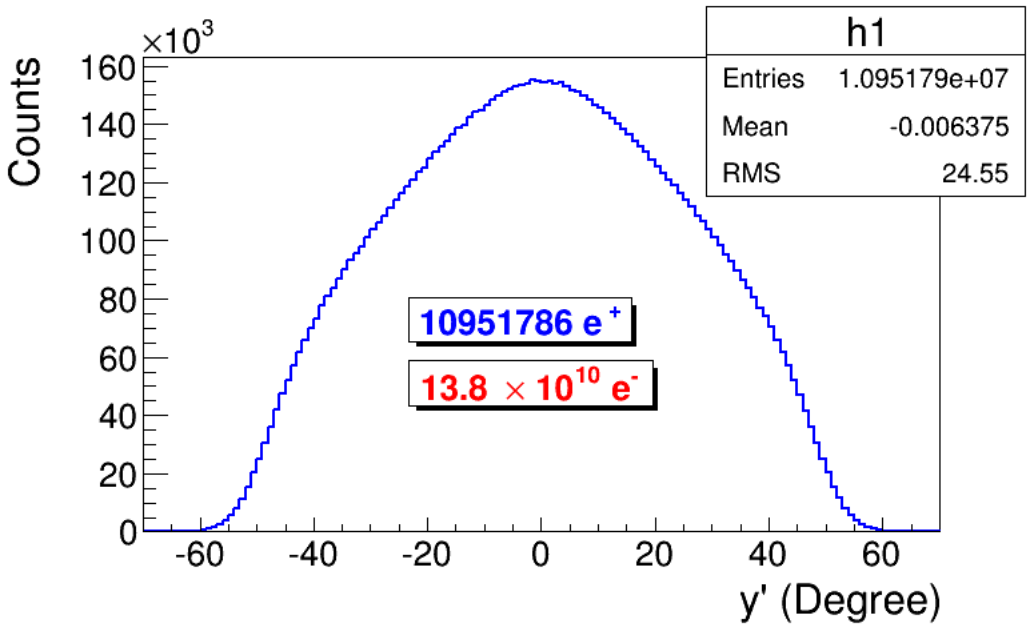

Figure 5.5: XP DDNT1

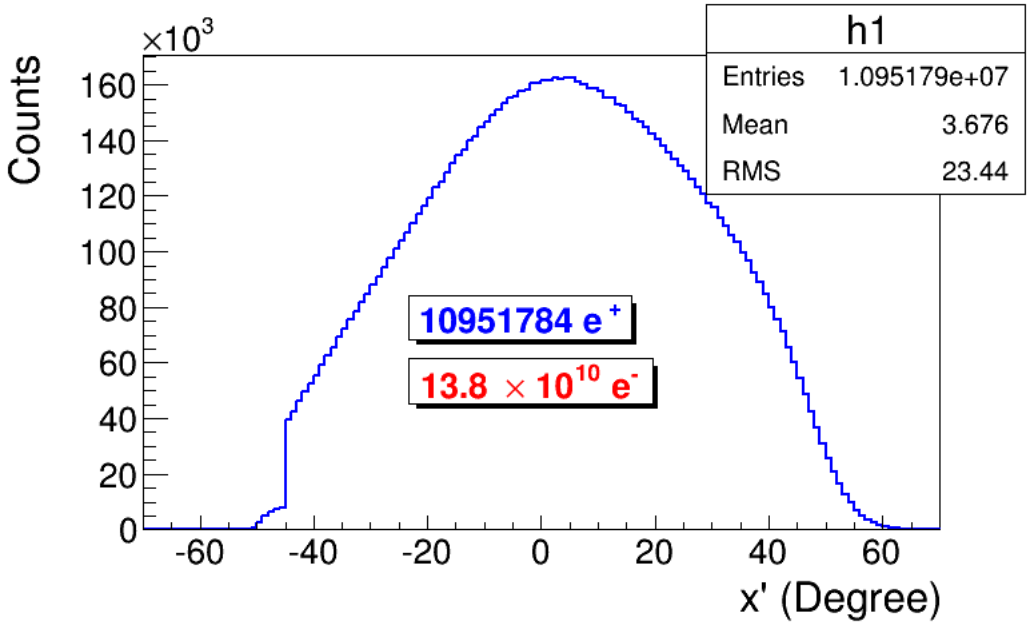

Figure 5.6: YP DDNT1

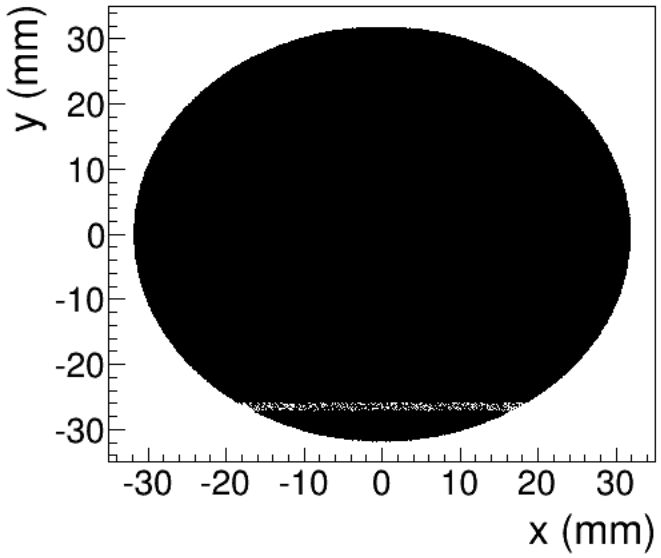

Figure 5.7: XY DDNT1

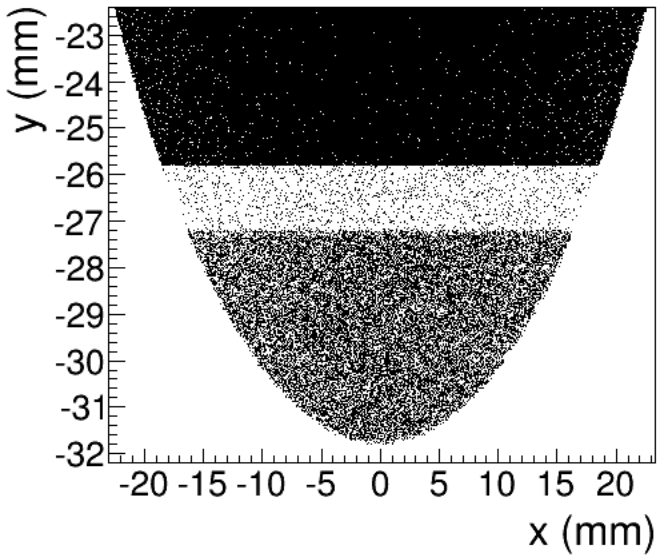

Figure 5.8: XY DDNT1 zoom

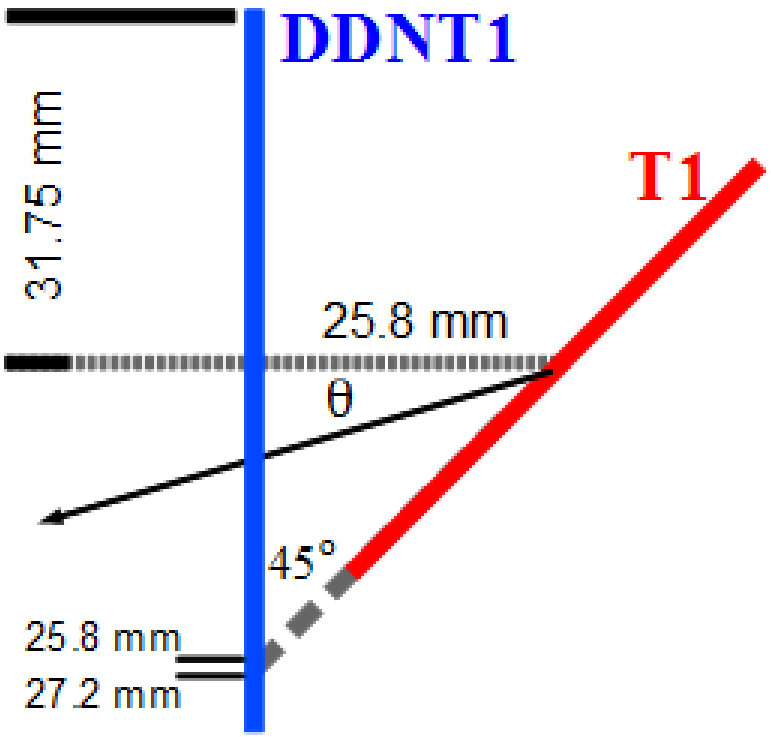

Figure 5.9: Geometry of the target T1 and the sensitive detector DDNT1

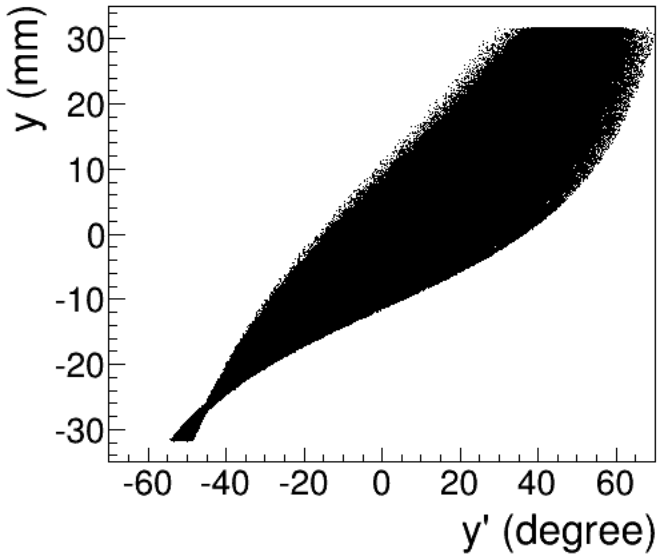

Figure 5.10: Y' vs Y.

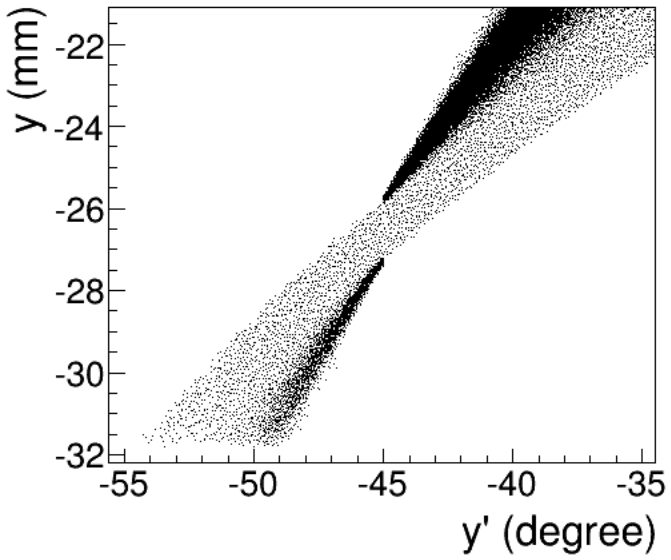

Figure 5.11: Y' vs Y zoom.

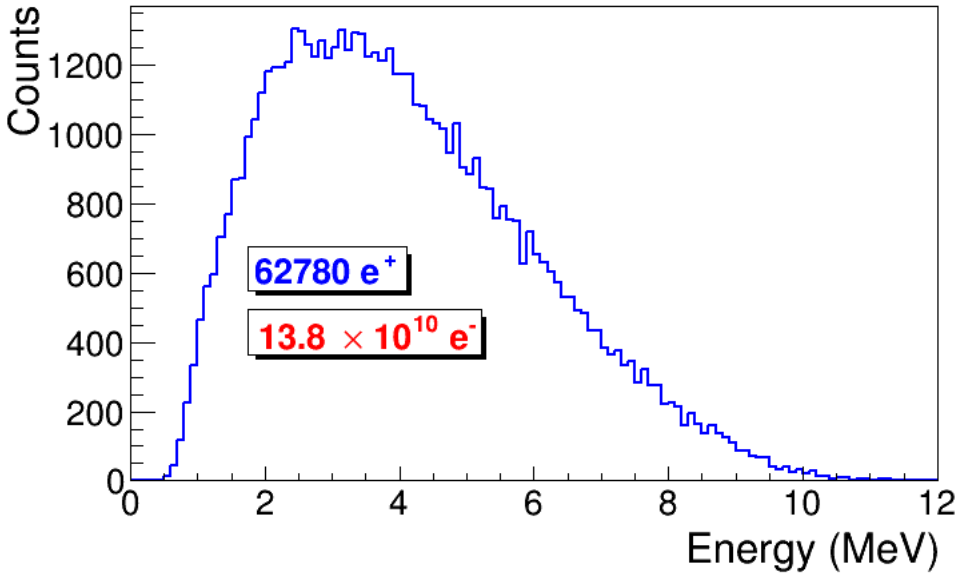

Figure 5.12: e+ Energy on DQ4

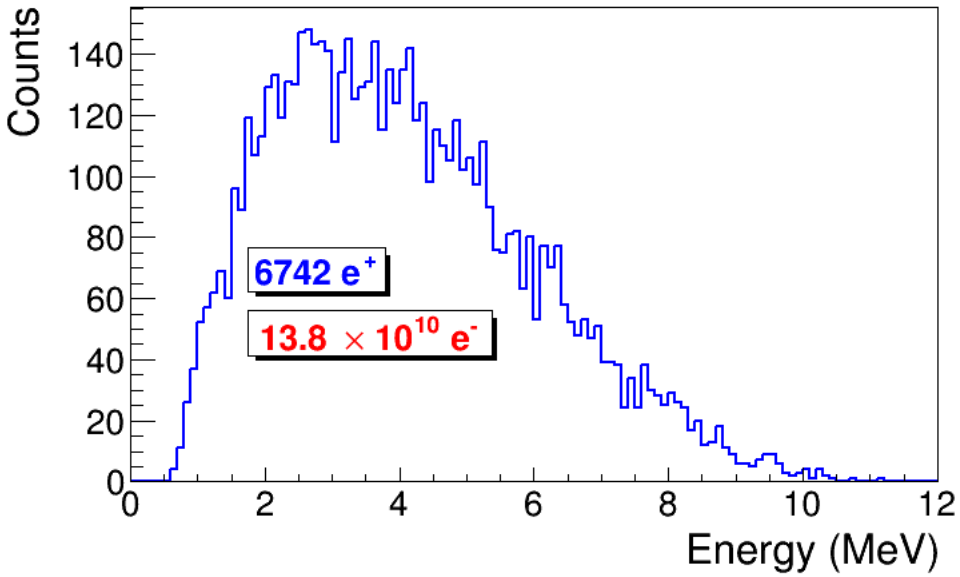

Figure 5.13: e+ Energy on DD1

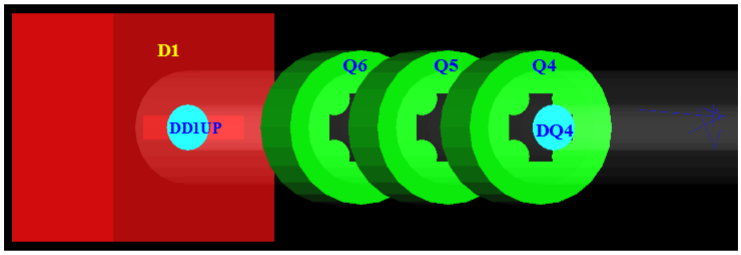

Figure 5.14: Step 2 setup.

Chapter 6

Conclusions

1. Reconfigured HRRL for positron production.

2. Constructed a positron detection system using two NaI detectors.

3. Experimentally measured positrons at different energies (1-5 MeV). Peak is around 3 MeV.

References

[1] S., Chemerisov. and C. D., Jonah, "Generation of high intensity thermal positron beams using a 20-MeV electron linac," *INTERNATIONAL WORKSHOP ON POSITRONS AT JEFFERSON LAB*, Newport News, Virginia, 2009.

[2] M. N. Rosenbluth, *Phys. Rev.*, 18, 1014 (1950).

[3] R. C.Walker *et al.*, *Phys. Rev. D*, 49, 5671 (1994).

[4] J. Arrington, *Phys. Rev. C*, 68, 034325 (2003).

[5] R. C. Walker, *Ph.D. thesis*, California Institute of Technology, 1989.

[6] K. S. Krane, *Introductory Nuclear Physics*, John Wiley & Sons, New York, 1988.

[7] NIST, *http://physics.nist.gov/cgi-bin/Xcom/xcom2*, NIST XCOM, 2013-05-03.

[8] M. Conte, and W. W. Mackay, *An Introduction To The Physics Of Particle Accelerators*, World Scientific, New York, 2008.

[9] K.T. McDonald and D.P. Russell, Fron. of Par. Beams Obser. Diag. and Cor. **08544**, (1988).

[10] Y. Kim *et al.*, in *Proc. FEL*2008, Gyeongju, Korea.

[11] S.Y. Lee, *Accelerator Physics*, (Singapore: World Scientific, 2004), 61.

[12] D.F.G. Benedetti, *et al.*, Tech. Rep., DAFNE Tech. Not., Frascati, Italy (2005).

[13] B. Gitter, Tech. Rep., Los Angeles, USA (1992).

[14] F.J. Decker, NASA STI/Recon Tech. Rep. N **1996**, (1994) 10487.

[15] , , , .

[16] , , , .

[17] , , , .

[18] , , , .

[19] , , , .

[20] , , , .

[21] , , , .

[22] , , , .

[23] , , , .

[24] , , , .

[25] , , , .

[26] , , , .

[27] S. Cook, "The complexity of theorem-proving procedures," *Proceedings of the 3rd ACM Symposium on Theory of Computing*, Shaker Heights, Ohio, 1971, pp. 151–158.

[28] M. R. Garey and D. S. Johnson, *Computers and Intractability: A Guide to the Theory of* NP-*Completeness*, W. H. Freeman, San Francisco, 1979.

[29] R. Karp, "Reducibility among combinatorial problems," in: R. Miller and J. Thatcher (eds.), *Complexity of Computer Computations*, Plenum Press, New York, 1972, pp. 85–103.

[30] R. B. Kearfott and V. Kreinovich (eds.), *Applications of Interval Computations*, Kluwer Academic Publishers, Norwell, MA, 1996.

[31] V. Kreinovich, A. V. Lakeyev and S. I. Noskov, "Optimal solution of interval linear systems is intractable (NP-hard)," *Interval Computations*, 1993, No. 1, pp. 6–14.

[32] V. Kreinovich, A. V. Lakeyev and J. Rohn , "Computational complexity of interval algebraic problems: some are feasible and some are computationally intractable: a survey," in: G. Alefeld and A. Frommer (eds.), *Scientific Computing and Validated Numerics*, Akademie-Verlag, Berlin, 1996, pp. 293–306.

[33] V. Kreinovich, A. V. Lakeyev, J. Rohn and P. Kahl, *Feasible? Intractable? On Computational Complexity of Data Processing and Interval Computations*, Kluwer Academic Publishers, Norwell, MA, 1996 (to appear).

[34] U. Kulisch and W. L. Miranker, *Computer Arithmetic in Theory and Practice*, Academic Press, NY, 1981.

[35] A. V. Lakeyev and V. Kreinovich, "If input intervals are small enough, then interval computations are almost always easy," *Reliable Computing*, Supplement (Extended Abstracts of APIC'95: International Workshop on Applications of Interval Computations), 1995, pp. 134–139.

[36] L. Levin, "Universal sequential search problems," *Problems of Information Transmission*, 1973, Vol. 9, No. 3, pp. 265–266.

[37] R. E. Moore, "Automatic error analysis in digital computation," *Technical Report LMSD-48421*, Lockheed Missiles and Space Co., Palo Alto, CA, January 1959.

[38] R. E. Moore, *Interval Analysis*, Prentice Hall, Englewood Cliffs, NJ, 1966.

[39] A. Neumaier, *Interval Methods for Systems of Equations*, Cambridge University Press, Cambridge, 1990.

[40] S. G. Rabinovich, *Measurement Errors: Theory and Practice*, American Institute of Physics, NY, 1995.